The Hebrew University of Jerusalem

The Faculty of Mathematics and Sciences

Department of Applied Physics

Nano Scale Charge separation using Chiral Molecules

Nir Peer

Under the Supervision of: Prof. Yossi Paltiel

Master degree of Science Thesis

July 2015

Acknowledgments

I want to thank many people who supported me throughout my entire project.

First, I would like to thank Yossi Paltiel for his guidance and support. His door was always open and he constantly had new ideas of how to approach different issues in my project and solve problems. I really appreciate his open-minded and friendly approach to his students, which creates the amazing collaborative atmosphere in the group and makes him an excellent mentor.

Second, I would like to thank Shira Yochelis for her imminent knowledge, her help and support with the theoretical knowledge and practical work in the chemistry lab. Her patience, and willingness to assist with any question I had during my degree helped and taught me in so many ways.

Last but not least, I would like to thank my friends in the lab for the support and for the great atmosphere that makes the lab a great place to be in. I would especially like to thank Oren Ben-Dor for sharing with me his knowledge and the lessons he already learned from previous successful and unsuccessful attempts in his research. His assistance really helped me to get started with my research and become independent in my work.

Abstract

Charge separation is a fundamental process currently being used in a large variety of optoelectronic devices, such as solar cells and photodetectors. A subset of these devices are photovoltaic devices, that is, charge-separating systems that are operated by light energy. In many of these devices charge separation requires doped P/N junctions that at the nano scale is limited due to the small number of atoms participating, thus becoming problematic when miniaturization is required.

In recent years, studies of electron transfer through organic chiral molecules have shown that these molecules can introduce quantum mechanical properties, such as discreet energy levels and electron spin selectivity, to the standard electronic components at ambient temperatures. It has been shown that chiral helical molecules can serve as efficient spin filters due to strong spin orbit coupling mechanisms and different scattering probabilities, thus creating a chiral-induced spin selectivity (CISS) effect.

Semiconductor nanocrystals (NCs), often called quantum dots can be used in photonic devices. Their versatility arises from the tunnability of optical and electronic properties with size, shape, composition among others. Utilizing semiconductor nanocrystals and the spin selectivity characteristics of electron transport through chiral molecules, we demonstrate nano scale charge separation using a thin layer device based on chiral molecules and semiconductor NCs. This was achieved by combining a self-assembled monolayer (SAM) of polyalanine with NCs and measuring different current responses under different polarized excitations. The NCs were excited with circularly polarized light, enabling the induction of charge separation in the chiral layer for large NCs.

Results show a significant difference in the current responses that was attributed to the CISS effect and to room temperature charge separation. Our devices can be fabricated in small scale and the size of the adsorbed NCs can provide optical tunability. In the future this technology may be used for active, charge separating coatings or smart sheets. Incorporating the NCs within chiral nano crystalized cellulose sheets was already demonstrated by me during my research.

Table of Contents

1. Introduction

1.1 Chirality and the chiral induced spin selectivity effect

Chiral molecules, molecules that lack mirror symmetry, have been the focus of attention since it was established that all organisms are built of molecules with specific handedness. The term chirality was first used by Lord Kelvin in 1893 in the second Robert Boyle Lecture at the Oxford University Junior Scientific Club which was published in 1894:

I call any geometrical figure, or group of points, 'chiral', and say that it has chirality if its image in a plane mirror, ideally realized, cannot be brought to coincide with itself. [1]

Chirality is essential in stereochemistry and biochemistry, for example natural sugars are all right handed and natural proteins are all left-handed.[2] This homochirality seen in nature is what inspired scientists to explore the implications and origin of chirality. The study of molecular chirality as a spin selective mechanism started to develop at the beginning of the 1980s. Preliminary theoretical work done by Farago[3] examined the consequences of electrons scattering from optically active molecules. Optical activated molecules are chiral asymmetric molecules that react differently to polarized light passing through them.

The work gave rise to three observable phenomena namely: (i) the attenuation of the electron beam depends on the longitudinal spin polarization of the incident beam (ii) an initially unpolarized beam emerges with longitudinal spin polarization and (iii) in the passage through the sample the transverse polarization of the incident beam undergoes a rotation about the beam axis.

These electron optic effects, like the optical ones, rest on the lack of inversion symmetry of the target molecules. The first phenomenon is the electron optic analogue of circular dichroism and the second is a direct consequence of this effect. The third is the analogue of the rotation of the plane of polarization of light by optically active media. This theoretical phenomena is clearly distinguishable from any Spin-orbit interaction effects, corresponding to Mott scattering (Polarized electron beam scattering off heavy atoms such as Gold), due to the lack of heavy atoms in the participating organic substance.

It was obvious that the lack of inversion symmetry, or parity violation, was related to the asymmetric structure of the target molecules. [4] Adjacent to Farago's theoretical work, calculations made by Rich for unpolarized electron beam elastically scattering from a chiral molecule, yielded a problematic electron helicity measurement, manifested as "helicity density". It was considered that Z=6 (atomic number of a carbon center) was the heaviest atom involved, thus a very small result could be obtained. [5] Theoretical predictions concluded different asymmetric behaviors: 1) For a fixed magnitude of longitudinal electron polarization the asymmetry magnitude will increase linearly with sample density, 2) Opposite isomers yield different asymmetry signs, 3) The asymmetry vanishes for an unpolarized electron beam or usage of racemic mixture (contains equal amounts of left and right handed molecules).

Initial experimental data focused on electron beam scattering off from camphor vapor ($C_{10}H_{16}O$), which is considered to be optically active under polarized illumination. Tests were conducted using a Mott polarimeter, measuring the scattering of polarized electrons. For an electron beam of polarization *P*, alternately parallel or antiparallel to the beam axis, the transmitted intensities $I(P)$ and $I(-P)$ yield a transmission asymmetry factor of $A=\frac{I(P)-I(-P)}{I(P)+I(-P)}$. The right-handed enantiomer's scattering result was $A(D)=(23\pm11)\times10^{-4}$ while for the left-handed enantiomer a $A(L)=(-50\pm17)\times10^{-4}$ result was seen. These results present clear difference within uncertainties of single standard deviation, and the difference of three standard deviations between measured values.[6] The difference between polarizations was larger than the theoretical prediction, thus generating a more profound experimental interest.

An attempt to reproduce the results was made by Mayer & Kessler [7], using similar experimental setup, but with a better apparatus. Even though experiments were made using wider electron energies in order to allow resonance scattering, the differences between L and D values did not exceed the given statistical errors, therefore failing to reproduce the former experiment's results. Nevertheless, an additional experiment using $Yb(hfc)_3$ yielded $A\sim10^{-4}$, with much smaller errors (Figure 1), which lies in good agreement with theory.

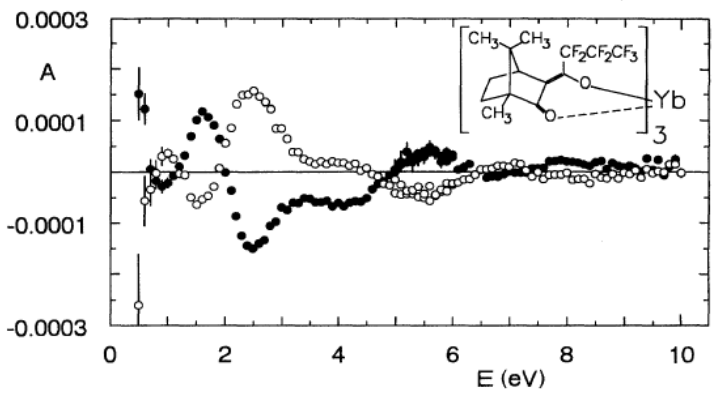

Figure 1: Transmission asymmetry A measured for D-Yb(hfc)3 (filled) and L-Yb(hfc)3 (open) vs. electron energy E. Error bars are visible whenever they are larger than the asymmetry symbols. The structure of D-Yb(hfc)3 is indicated in the inset.[7]

Apparently, incorporation of the heavy ytterbium with an atom number of Z=70, within a chiral structure, gave a way to stronger SOC – thus stronger dichroism.

Several attempts to find a chiral structure that would substantially increase the asymmetry factor were made[8], until a surprising breakthrough came in 2011[9] when spin polarizations, for photoelectrons transmitted through double strand DNA (dsDNA) at RT, exceeded 60%. It was the first time that such large polarizations were measured even though the dsDNA is constructed out of light atoms indicating a weak SOC. The experiment consisted of self-assembled monolayer (SAM) of dsDNA adsorbed on a Gold substrate. The surface was illuminated by UV pulse laser incident light normal to the sample, illuminating with linear or circularly polarized light and ejecting photoelectrons from gold substrate (Figure 2).

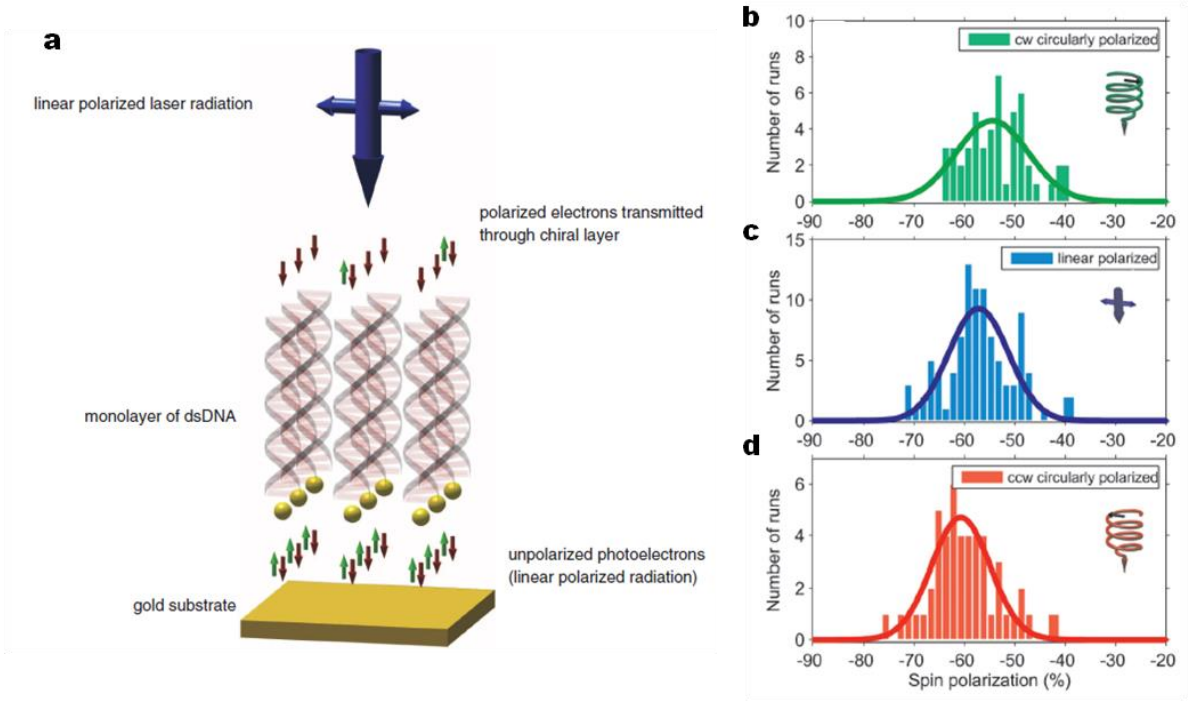

Figure 2: A scheme describing the monolayer of dsDNA as spin filter. **a.** Unpolarized electrons are ejected from the gold substrate by a linearly polarized light. Most of the electrons transmitted through the DNA are polarized with their spin aligned anti-parallel to their velocity. The electrons that are not transmitted are captured by the DNA and tunnel back to the grounded substrate within the time period between two laser pulses. Results are displayed for electron polarization for CW circularly polarized light (**b.** green), linearly polarized light (**c.** blue) and CCW polarized light (**d.** red).[9]

The polarized photons are coupled to the subsequent emitted photoelectrons' spins, so for right-handed polarized light illumination a photoelectron with right-handed spin polarization is emitted and vice versa. Photoelectrons emitted from the Gold substrate were transmitted through the monolayer towards the Mott polarimeter, where their spin polarization is analyzed. Different light polarizations were investigated, including left-handed, right-handed and linear polarizations. For 50 base pairs (bp) dsDNA a polarization of $\sim(-32\%)$ was measured with negligible differences between clockwise (CW), counterclockwise (CCW) and linear polarization measurements, suggesting a very strong spin selectivity effect. For 78bp dsDNA, a polarization of $\sim(-58\%)$ was obtained again, almost regardless of the light polarization. For single strand DNA (ssDNA) no polarization was observed.[9,10]

Another important experiment published at the same year demonstrated selective spin conductivity measurements of spin transfer through a chiral SAM of dsDNA attached at the top with 10nm Gold nanoparticles. The molecules were adsorbed on

a 200nm Ni substrate that is magnetized by a permanent magnetic field of ~0.3 Tesla. An atomic force microscope (AFM) measured the transport of electrons through the Gold nanopatricles attached on top of the dsDNA molecules to/from the bottom magnetized Ni substrate. Samples with different molecule lengths were measured, consisting of 26, 40 and 50 dsDNA bps. As expected, different I-V curves were measured for both parallel and anti-parallel (to the molecules major axis) magnetic fields as well as for different lengths. This is a clear indication that indeed dsDNA acts as a spin filter. Once again the molecule length is a major factor of the spin polarization capability.[11]

These two experiments supply proof that there is no need for strong SOC originating from heavy atoms. The spin filtering and polarization is more affected by the chiral and helical molecular structure. It is important to note that the measurements were made at room temperature. My work is using the established evidence that SAM of chiral molecules, such as dsDNA, can provide a very effective spin filter at RT, to develop spintronic applications.

1.2 Nano Crystals

Quantum confinement was first observed by Faraday on nano particles of gold[12]. He dispersed particles of gold in a liquid preparing so-called colloids of gold. The color of the colloid ranged from vivid red to blue, depending on the sizes of the dispersed particles of gold. Similarly, while the bulk direct-gap semiconductors' fluorescence wavelength is determined by the material, nanoparticles of the same material may emit at different wavelengths depending on their sizes. Quantum confinement effect modifies the energy levels of the material and changes its optical and electronic properties. The valence as well as the conduction energy band splits into discrete energy levels near the bulk energy gap and a continuum far from the energy gap. The nanoparticles with such an energy structure are called quantum dots. They are often referred to as "artificial atoms" because their atom-like discrete energy levels are size-dependent, i.e. tunable. An excited state of a quantum dot corresponds to a creation of an electron in a conduction level and a hole in a valence energy level. The electron-hole pair is also called exciton. In a direct-gap semiconductor quantum dot, the electron-hole pair may recombine radiatively emitting a photon.

1.3 Charge Separation

Charge separation is essential for large variety of optoelectronic devices, such as solar cells and photodetectors.[13] A subset of these devices are photovoltaic devices, that are charge-separating systems operating by light energy.[14] Nowadays, these systems are mainly based on doped silicon, in which a junction is formed between a donor dopant (p-type) and an acceptor dopant (n-type). Charge diffusion equalizes the Fermi energy of both layers creating an electric field called the "depletion region" that has a built in potential. Under an applied bias voltage and above bandgap illumination, the device will create an electron-hole pair that will be separated according to the built-in potential. One of the main drawbacks in these devices arises when miniaturization is required, since the amount of doping in a semiconductor is limited to the maximum concentration of $10^{19}\frac{dopants}{cm^3} = 10^{-2}\frac{dopants}{nm^3}$, over which the material is considered degenerate at room temperature.[15] This means that typically there is less than a single dopant per cubic nanometer, thus making it almost impossible to create a doping-controlled charge separation at the nanoscale.

In my work I demonstrate nano scale charge separation using a thin layer device based on helical chiral molecules and semiconductor NCs. We combined a SAM of polyalanine with NCs and measured the induced photocurrent when the NCs are illuminated with light polarized in different ways. By applying circularly polarized light it was possible to generate charge separation in this system.

2. Scientific Background

2.1 Chirality and Helicity

Objects are chiral (from Greek “cheir” means “hand”) if they exist in two non-superimposable forms that are each other’s mirror image, like our hands.[16] The word Chirality was first introduced by Lord Kelvin in order to describe a chiral geometrical figure or object:

“If its image in a plain mirror, ideally realized,
Cannot be brought to coincide with itself”

In quantum mechanics, the invariance of the Hermitian conjugate of the Hamiltonian H yields conservation laws or selection rules which are important for physical processes' deeper understanding. Two symmetry operations corresponding to distinct inversion are especially fundamental, namely parity and time reversal (a third operation named charge conjugation is not in the scope of this background). Chiral molecules break parity symmetry; however, they retain time-reversal symmetry, and it is necessary to have a charge flowing through them in order to break time-reversal symmetry and thus meet the symmetry requirements for generating a magnetic field along the charge’s velocity direction [17].

2.1.1 Chirality – spin filter

As mentioned in the introduction, recent electron transmission experiments have shown unequivocally that ordered films of chiral organic molecules on surfaces can act as electron spin filters at room temperature, an effect that is termed the chiral-induced spin selectivity (CISS). The experiments were followed by extensive theoretical experimental work in order to study the CISS effect. As of today many opened questions have remained unsolved, however successful advances were achieved and produced new important insights.

There are several works that investigated the CISS effect from a theoretical perspective [18–21], and the methods used can be divided into three categories. In one

approach, tight binding models were used to describe electron transmission through large helical molecules, such as DNA and oligopeptides [11,22–25]. Another approach used spin-dependent scattering theory to obtain spin-dependent electron transmission[21]. In a third approach, models that include a large SOC from the metal substrate give rise to spin selectivity via angular momentum selection.[26]

Despite the differences in their methodology, the results show that the chiral layer acts as a spin filter. The tight binding models are based on spin orbit coupling (SOC) interactions calculation using the Rashba SOC term H_{SOC} in a helical potential. SOC generally grows with atomic number Z as $H_{SOC} \propto Z^4$ (for hydrogen-like atom). Organic materials such as C, N, O and H normally consist of low-Z materials, thus SOC is expected to be lower in organic materials, although not insignificant. Despite the expected low SOC per atom, due to low mobility electrons spend larger times in proximity to the atoms, thus generating significantly higher SOC value than that found in standard Z atoms ($\sim 3.6\ meV$ for a free carbon atom). Nevertheless, the full understanding of the unusually large effective SOC of chiral molecules, hundreds of milli–electron volts in DNA[11], is not explained by a quantitative theory. In the models it is rationalized in terms of the molecules' secondary structure, e.g. the alpha helix molecular and DNA structures. However, no detailed model exists that relates those molecular characteristics directly to the spin polarization and only a phenomenological model can predict to a full extant the experimental results.

2.1.1.1 Spin orbit coupling term in chiral molecules – a simple model

The model consider a simplified model of a helical molecule such as alpha helix (see Figure 3), in order to estimate the nature of the SOC term in chiral molecules. As an electron moves along a chiral molecule, it experiences the electrostatic potential of the molecule, which is also chiral.

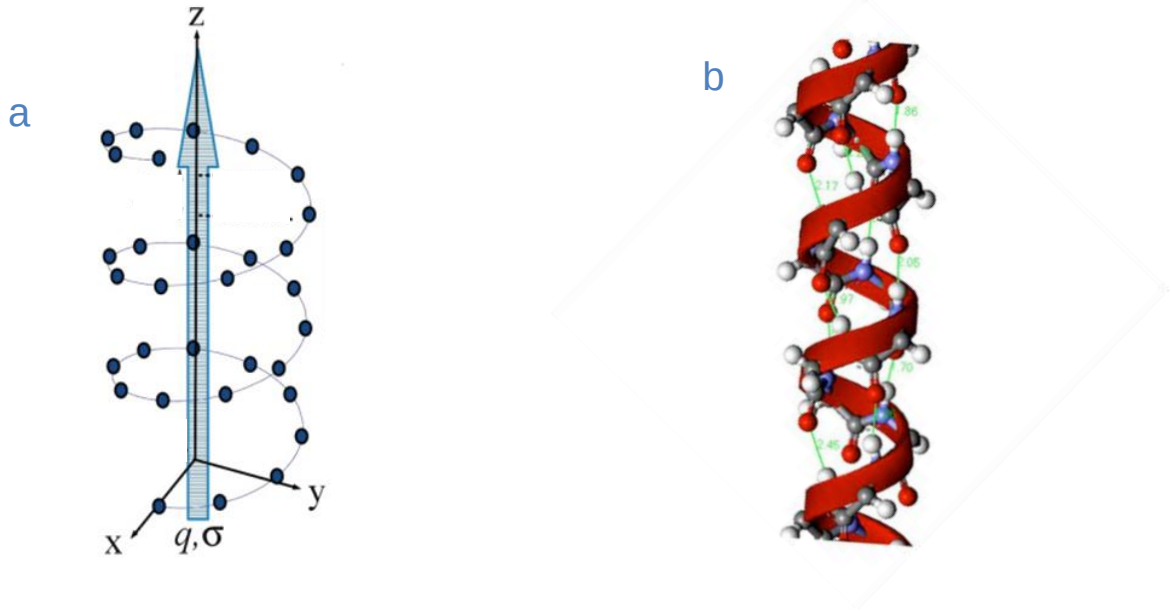

Figure 3: a – An illustration of a helical molecule with point charges representing the atoms along the helical path. b- Side view of polyalanine with ***α*** helix structure. grey: carbon, white: hydrogen, blue: nitrogen, red: oxygen

In the electron's rest frame, the current generates a magnetic field $\vec{B}$:

$$\vec{B} = \frac{\vec{v}}{(2c)^2} \times \vec{E}_{chiral}$$

In which $\vec{v}$ is the velocity of the moving electron, c is the speed of light, and $\vec{E}_{chiral}$ is the electric field acting on the electron while it moves through the chiral molecule and it is caused by the electrons and nuclei along the chiral molecule. The factor of 2 is a correction for relativistic effects.[27] Taking standard values, of a relativistic electron propagating with a speed of $0.002c$, experiencing an electric field of $\vec{E}_{chiral} = 4.5 \cdot 10^{11}\ V/m$, it would generate a magnetic field of 3T.[28]

Because the electron has a magnetic dipole associated with its spin, the two spin states that are degenerated when no magnetic field exists are now split. The interaction between the spin value and the magnetic field induced by the motion of the electron in a chiral potential is given by the SOC term [29] in the Hamiltonian:

$H_{SO} = \lambda\vec{\sigma} \cdot \left(\vec{p} \times \vec{E}_{chiral}\right)$, in which $\lambda = \frac{q\hbar}{(2mc)^2}$, $\vec{p}$ is the electron's momentum, m is the electron's mass and $\vec{\sigma}$ is a vector whose components are the Pauli matrices $(\sigma_x, \sigma_y, \sigma_z)$. For convenience H_{SO} is written as:

$$H_{SO} = \frac{1}{h}\vec{\sigma} \cdot (\vec{p} \times \vec{\alpha})$$

In which $\vec{\alpha} = \hbar\lambda\vec{E}_{chiral}$.

The energetic split of two opposite spin values is therefore:

$$\Delta H_{SO} = \frac{1}{h}(\vec{p} \times \vec{\alpha})$$

We can see that the energetic split is dependent on the strength of electric field, but would also be opposite for different handedness of the chiral molecule. It is also dependent on the electrons propagation direction $\vec{p}$ and the sign of the charge propagating, as seen in the λ definition, and will be opposite for electrons or holes transferring through a chiral molecule.

2.1.1.2 Energy levels in the CISS effect

As demonstrated previously, chiral potential causes a significant coupling between a particle's linear momentum and its spin, even when SOC is small (e.g. in organic materials). This coupling has an important implication for the efficiency of charge transport in the molecular helix.

Taking into account an electron propagating in a chiral potential, we can denote four states in the form $|\vec{v},\ \vec{s}\rangle$, in which $\vec{v}$ indicates the electrons propagating direction (as well as the momentum $\vec{p}$) along the $\hat{z}$ axis, and $\vec{s}$ indicates the spin direction along the $\hat{z}$ axis. Finally, we can apply the SOC Hamiltonian to describe the different energy

levels for all electron states, in right or left handed chiral molecule potential as seen in Figure 4.

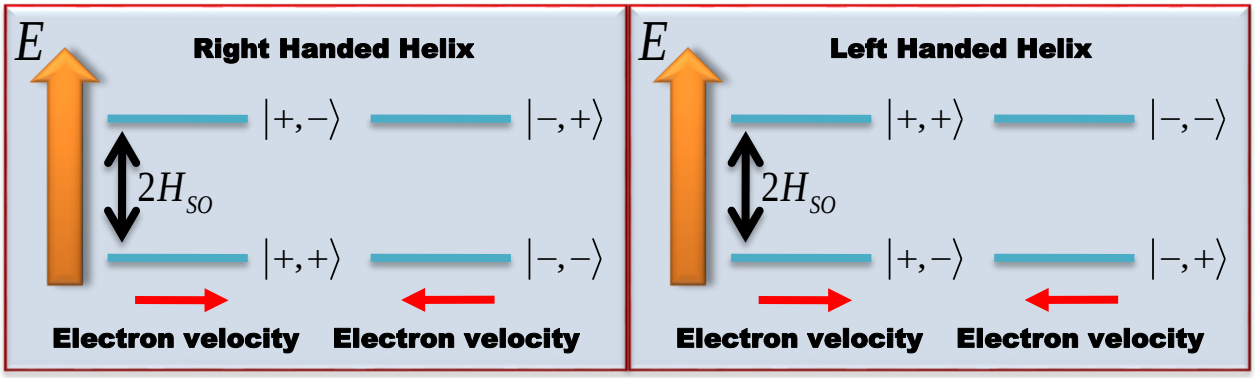

Figure 4: An energy scheme depicts the |**Momentun**, **Spin**⟩ states of an electron moving within a chiral potential, for left and right handed helices.

An electron moving in the (+) upwards direction through a right-handed helix, its spin up (+) parallel to its velocity, has lower probability for scattering relative to its down spin (-); that is, $|\vec{+}, \vec{+}\rangle$ is the ground state, and the state $|\vec{+}, \vec{=}\rangle$ lies at higher energy gap of $2H_{SO}$. Furthermore, the $|\vec{+}, \vec{+}\rangle$ state is degenerate with the $|\vec{=}, \vec{=}\rangle$ state, which corresponds to the electron moving in the opposite direction with opposite spin. Similarly, the $|\vec{+}, \vec{=}\rangle$ state which lies at higher energy is degenerate with the $|\vec{=}, \vec{+}\rangle$ state (Figure 4). For an electron to be elastically backscattered within a helical molecule, it has to change its state from $|\vec{+}, \vec{+}\rangle$ to$|\vec{=}, \vec{=}\rangle$, which requires a change in spin as well as momentum, thereby making it unlikely. Another option is to scatter from the $|\vec{+}, \vec{+}\rangle$ state to the $|\vec{=}, \vec{+}\rangle$ state which requires additional energy and therefore a gap for scattering is formed. When conducting experiments at room temperature (RT), thermal distribution of electron energies has to be taken into account when discussing a backscattering possibility. For an electron to be backscattered while maintaining its original spin orientation, it has to acquire energy exceeding $2H_{SO}$, in order to populate a higher-lying momentum-spin state (i.e. $|\vec{=}, \vec{+}\rangle$ in the above example). The fraction of the population that has energy exceeding the energy of the $|\vec{=}, \vec{+}\rangle$ state is given by $V_{bs} = \exp\left(-\frac{2H_{SO}}{KT}\right)$ thus for $H_{SO} = 20\ meV$, which is a typical theoretical result, about 20% of the population (at RT) will have enough energy to backscatter with no spin-flip, namely, the backscattering cross section will be reduced by a factor of about 5. Experimental results in DNA oligomers indicate

that elastic backscattering that does not include spin-flipping is highly improbable.[30] Thus from an energy perspective the CISS effect reduces dramatically back scattering.

2.2 Nano Crystals

Semiconductor nanocrystals (NCs) are nanometer-sized crystalline particles that contain approximately 100 to 10,000 atoms. With the use of chemical syntheses, they can be fabricated with almost atomic precision as nearly spherical nanoparticles (quantum dots)[31,32], elongated nano-sized crystals (quantum rods)[33], or nanostructures of other more complex shapes such as tetrapods[34]. The ability to precisely control the composition, size, and shape of NCs provides great flexibility in engineering their electronic and optical properties by directly manipulating electronic wave functions (wave function engineering). In this work I used CdSe quantum dots, which are spherical and have a wurzite crystal structure.

2.2.1 Bandgap of NCs

Direct-gap semiconductors can absorb a photon when an electron is promoted directly from the valence band into the conduction band.[35] The photon will be absorbed if its energy ($E_{photon} = h\nu$) is higher than the energy gap size E_g of the semiconductor, then an electron–hole pair (exciton) will be created in the material. In bulk semiconductors, the strength of the electron–hole (e–h) Coulomb interaction of an exciton determines a natural length scale defined as the exciton Bohr radius a_x.

If the size of the semiconductor structure becomes comparable to or smaller than a_x, the carriers start being confined by the boundaries of the material. This phenomenon, which is known as the quantum size effect, leads to atomic-like optical behavior in NCs and the bands become quantized (Figure 5).[36]

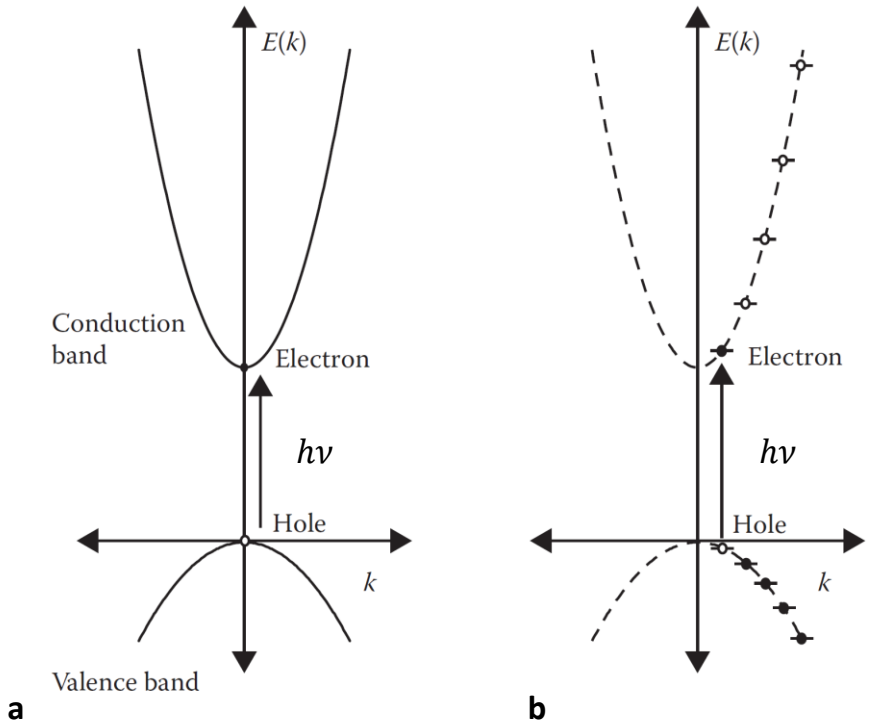

Figure 5 : (a) A band gap for a simple two band model for direct gap semiconductors. (b) Allowed optical transitions in semiconductor NCs, which become discrete due to the quantization of the bulk bands.

In NCs, a simple model of a spherical quantum well with infinite barrier can be applied, in which the NC energy gap $E_g(NC)$, is comparable to the bulk semiconductor energy gap, $E_g(bulk)$, by the following expression:

$$E_g(NC) = E_g(bulk) + \frac{\pi^2 \hbar^2}{2m_r R^2}$$

Where R is the NC radius, $m_r = \left(m_e^{-1} + m_h^{-1}\right)^{-1}$, and m_e and m_h are the electron and hole effective masses, respectively. It is apparent from this model that the energy gap E_g can be tuned. Usually it is easy to increase the bandgap by using smaller radius sizes of the same NC. In practice, it can be tuned by more than 1 eV for many different compositions. This can be used for controlling the emission color and the absorption and excitation spectrum.

2.2.2 Spin states in CdSe NCs

As mentioned before, a distinct feature of crystals smaller than 10nm is the discrete structure of energy levels that replace the continuous energy bands of a bulk material, as seen in Figure 6.

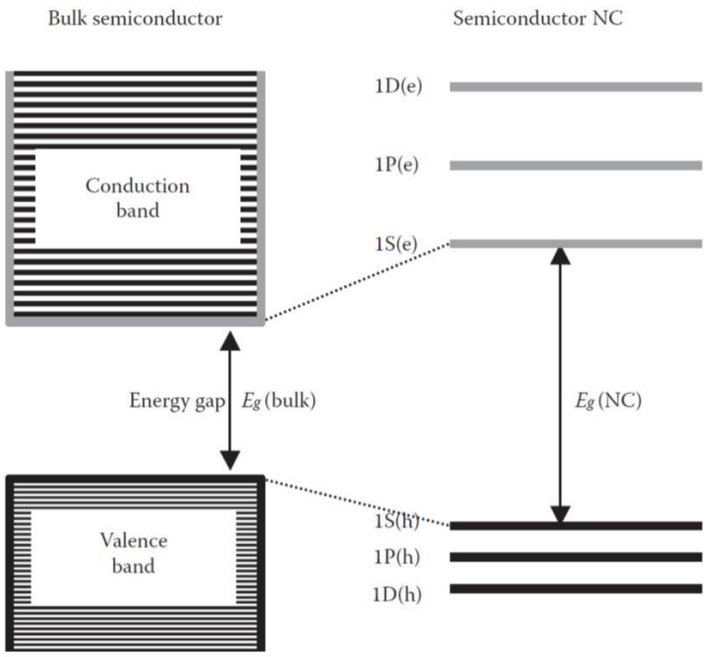

Figure 6: A bulk semiconductor has continuous conduction and valence energy bands separated by a fixed energy gap $\boldsymbol{E_g}$, whereas a semiconductor NC is characterized by discrete atomic-like states and an NC size-dependent energy gap $\boldsymbol{E_g(NC)}$

In the absence of band-mixing effects, each bulk band gives rise to an independent series of quantized states that can be classified using two quantum numbers[37]. One, L, determines the angular momentum of an envelope wave function and the other is the principle quantum number n. In the typical notation of NC quantized states, the momentum, indicated by a letter (S for L = 0, P for L = 1, etc.), is preceded by the value of n. The three lowest energy states in the order of increasing energy are 1S, 1P, and 1D (Figure 6). Most of our NC excitations in this research occur in the lowest 1S energy level.

This simplified model of NC electronic states shown in Figure 6 provides a reasonable description of the NC conduction band. However, because of the complex, multi-subband character of the valence band that is typical for many semiconductors, the NC valence-band structure can only be understood by taking into consideration

confinement-induced mixing between different subbands. In bulk wurtzite lattices, the lowest energy conduction minimum is formed from the S-type orbitals and is twofold degenerate due to the electron spin. The valence band formed from the P-type orbitals is sixfold degenerate. Because of the spin–orbit interaction, the valence band is split into a fourfold degenerate band with the angular momentum J = 3/2 and a twofold degenerate band with J = 1/2 (Figure 7). The energy separation between these bands, Δ_{so}, is determined by the strength of the spin–orbit interaction. In bulk semiconductors, the J = 3/2 bands is further split into light- and heavy-hole subbands with J projections J_m = ±1/2 and ±3/2, respectively.

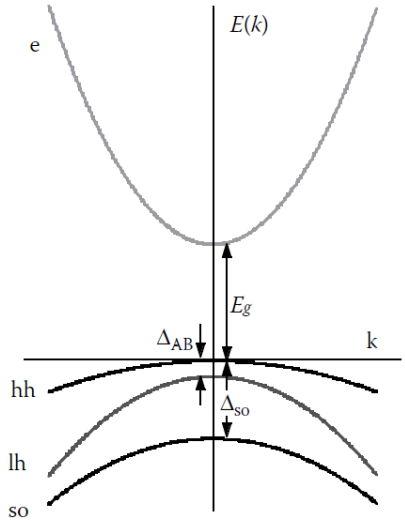

Figure 7: Conduction S-type band and valence P-type band structures in wurtzite bulk semiconductors. The valence band is composed of heave (hh), light (lh), and spin orbit split-off (so) subbands.

In the case of CdSe NCs there's a strong spin–orbit coupling applicable, in which the hole can be treated as a particle with spin 3/2 [38]. The lowest energy of the hole states in this case is $1S_{3/2}$. Therefore, we'll take into consideration the $1S(e) - 1S_{3/2}(h)$ transition which is the most probable and energetic efficient transition. In the presence of strong e–h exchange, the lowest energy $1S$ electron and $1S_{3/2}$ hole states, which are characterized by angular momenta 1/2 and 3/2, are considered as a single state of an exciton with a total angular momentum, J, of either 1 or 2. These two states are split by the exchange interaction forming a high-energy optically active $J = 1$ bright exciton and a lower-energy optically passive $J = 2$ dark exciton (Figure 8).[39]

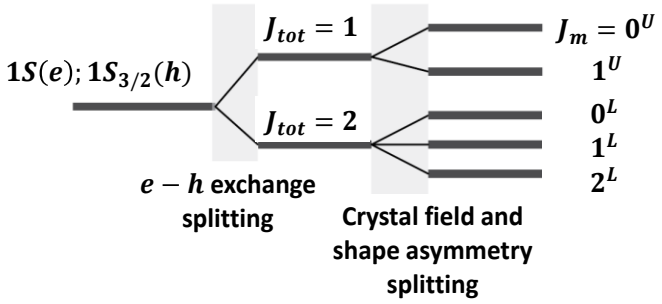

Figure 8: the $1S(e); 1S_{3/2}(h)$ transition. The state is splitted initially because of the electron-hole interaction, and further splitted to five sublevels because of the anisotropy of the CdSe wurtzite lattice.

These states are further split into five sublevels because of the anisotropy of the wurtzite lattice and the nonspherical CdSe NC shape, forming two manifolds of upper ("U") and lower ("L") fine-structure states, as seen in Figure 8. These states are labeled according to their projected total angular momentum values J_m. The effect of additional level-splitting does not change the nature of the lowest energy state, which remains optically passive and is characterized by $J_m = 2^L$. It is separated from the next, higher-energy $J_m = 1^L$ bright state by the energy of ~1 meV to more than 10 meV, depending on NC size. [40]

2.2.3 Spin values in the $1S(e); 1S_{3/2}(h)$ excited state

The total angular momentum J_m translates to the projected spin states values of the electron and hole $J_m = S_e + S_h$, with $S_e = \pm 1/2$ the spin states of the electrons and $S_h = \pm 1/2, \pm 3/2$ the spin states of the holes. Since photons have angular momentum of $m = \pm 1$ depending on the circular polarization of the light, the optically active states in the CdSe NCs are $J_{\mathrm{m}} = 1$. In these states the excitons have a particular spin alignment depending on the helicity of the light with the possible spin states of $(S_e, S_h)_{\pm 1/2, \mp 3/2}$ (with $J = \mp 1$). However, these states aren't in the lowest energetic level, a fast spin relaxation process occurs, in which the states decay to the lower dark $J_m = 2$ states (see Figure)in CdSe dots.

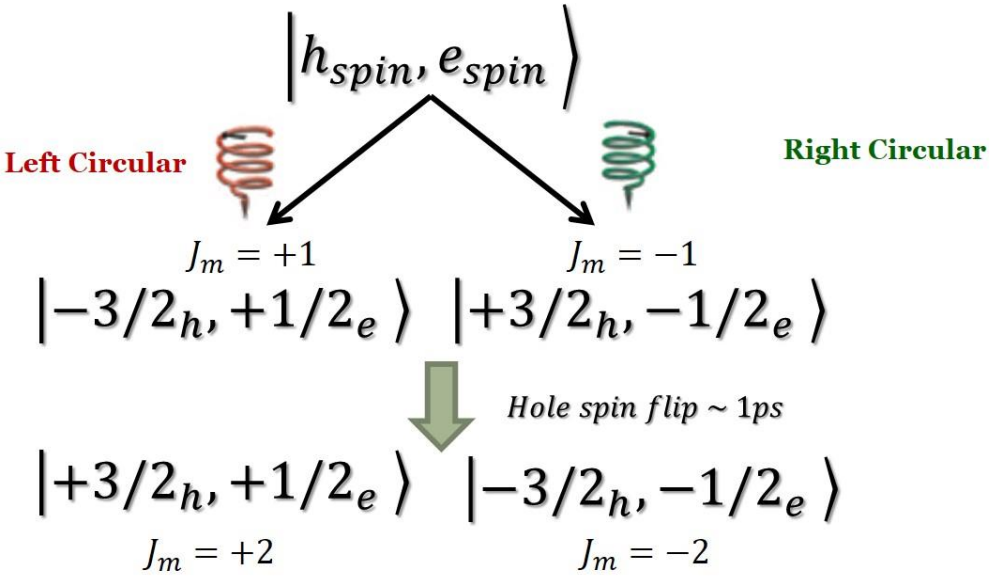

Figure 9: A schematic discription of the spin states decay in the $\mathbf{1S(e)}; \mathbf{1S_{3/2}(h)}$ state, depending of the circular polarization of the excitation. Both cases will decay to electron-hole states holding the same spin value, positive or negative for right or left circular polarization respectivly.

Exciton spin relaxation can be understood as the exciton interlevel or intralevel transitions among the exciton fine structures [41]. However, the characterization of the spin relaxation mechanism in NCs is still an open subject. Previous studies of exciton spin dynamics in quantum wells revealed that there are two predominant mechanisms to mediate the exciton spin relaxation - one is a direct (or say single-step) spin flip between the J = ±1 exciton states[42] the other is indirect spin flip, in which electron and hole flip their spin independently. [41] It is usually thought that the direct spin flip process is driven by the long-range term of the electron–hole exchange interaction,[43] and the indirect spin flip is governed by strong spin–orbit coupling in NCs.[42] Previous experiments on CdSe NCs show a fast spin relaxation which is attributed to an exciton interlevel transition in which the hole spin is flipped and electron spin is conserved. These experiments showed that for small CdSe NCs (with the diameter of 4 and 2.4 nm) another slow spin relaxation was observed besides the fast hole spin flip. This slow decay was attributed also to exciton intralevel transition in which the electron spin was flipped in NCs. [44]

The slow hole spin flip can be shown as a process of the decay of the optically excited states $(S_e, S_h)_{\pm 1/2, \mp 3/2}$ (with J = ∓1), to the states $(S_e, S_h)_{\pm 1/2, \pm 3/2}$ (with J = ±2) [44,45] as seen in Figure 9. In these final states electron and holes have the same sign to their spin values.

2.3 Self-Assembly Monolayer (SAM)

SAMs are created by the chemisorptions of the "head groups" onto a substrate, followed by a slow organization of the "tail groups". Initially, at small molecular density on the surface, adsorbed molecules form either a disordered mass of molecules or an ordered two dimensional form, and at higher molecular coverage, over a period of minutes or hours, begin to form three dimensional crystalline or semi crystalline structures on the substrate surface (Figure 10). Areas of close-packed molecules nucleate and grow until the surface of the substrate is covered in a single monolayer. Adsorbate molecules can be ordered readily because they lower the surface free energy of the substrate and are stable due to the strong chemisorption of the "head groups".

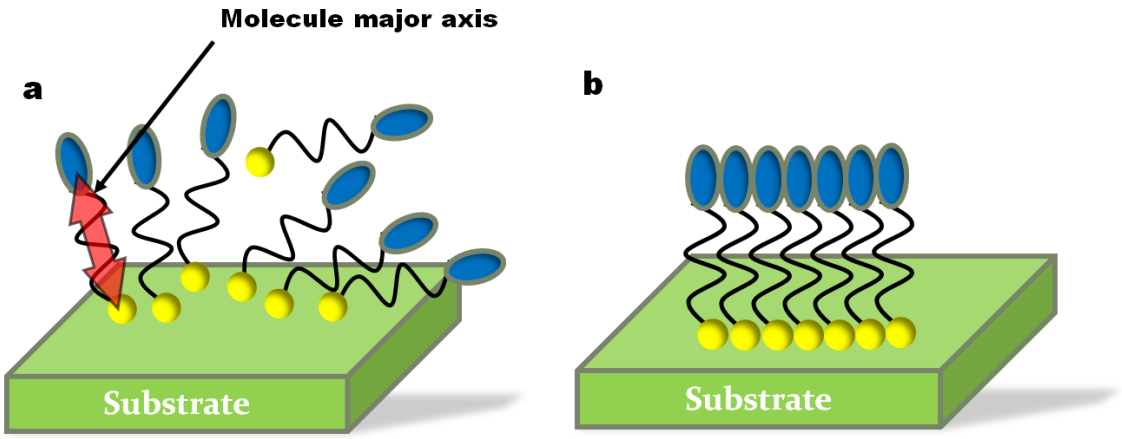

Figure 10: SAM adsorption method stages scheme. **a.** At the initial stage the molecules appear in a disordered manner while "head groups" start to create bonds with the substrate. **b.** After minutes or hours, ordered structures appear as the "tail groups" are closely packed and aligned.

Self-assembly of monolayer is used whenever a concentrated thin organic layer is required. One use of these layers can be achieved by driving current amid two conductive metals, through SAM sandwiched in between .[11] Using chiral molecules Self Assembly Monolayers' studies conducted with α Helix Polyalanine yielded a stable helical structure[46] that enabled adsorption on metal surfaces. In recent years a better understanding of these molecules' behavior has been accomplished due to better characterization methods. Essentially, it was found that the Polyalanine possesses a large magnetic dipole before adsorption but after the molecules' are attached a substantial decrease in the magnetic dipole occurs which facilitates their

close packing. The magnetic properties of the Polyalanine are probably related to their chiral behavior that is the reason for the large spin selectivity in electron transmission, an effect that results from the cooperative nature of the film on the metal substrate.[47]

3 The experimental system and measuring methods

3.1 The optical - electrical measurement setup

In my research most measurements were transport I-V measurements, in which the voltage was regulated with a Keithley 2400 Sourcemeter, and the current was measured with a Keithley 6485 Picoammeter. For part of the measurements we used a nano-voltmeter Keithley 2182A to measure the voltage response to illumination.

Transport behavior was studied under a polarized illumination, mostly with a diode-pumped solid-state continuous-wave (DPSS CW) 532 nm laser with max power of 50 mW. Typical power density used was 20 mW. For control measurements a 660 nm laser was used. Laser intensity was monitored by intensity detector to ensure power stabilization. The right/left circular polarization illumination (RCP/LCP) was achieved using a linear polarizer in the optical path (45° or 315°, accordingly) followed by a quarter wave plate with fast axis parallel set to 0° (see Figure 11). A simple mechanical shutter was placed along the optical path to compare light and dark measurements.

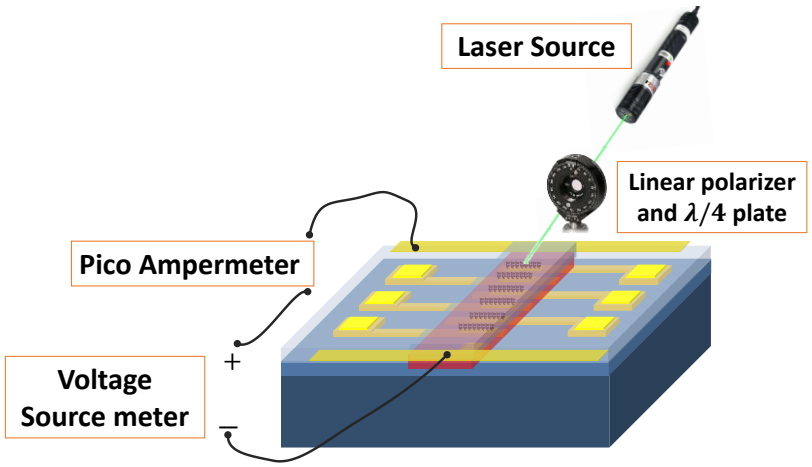

Figure 11: A schematic drawing of the setup of the electrical measuring system upon excitation with circularly polarized light.

Some of the measurements were performed in low temperatures of $55°K$. They were made in an Oxford Instruments CryoFree spectromag cooler, with the capacity of working between $1.5°K$ (base temperature) to $300°K$.

3.2 Adsorbed molecules and NCs characterization

In order to follow the SAM formation and effectiveness, different characterization methods were used to analyze the monolayer height. Polarization Modulation – Infrared Reflection Absorption Spectroscopy (PM-IRRAS) measurements were performed in order to define the tilt angle of the molecules relative to the surface normal. Atomic force microscopy (AFM) measurements were made to define the surface topography and to measure the thickness of the monolayer.

3.2.1 PM-IRRAS measurements

The structure and tilt angle of the molecules relative to the surface normal were determined by their PM-IRRAS spectra. In helical peptides such as the α helix molecules we used, the transition moment of amide-I band lies nearly parallel to the helix axis and that of amide-II perpendicular. Since transition moments, which lie parallel to the gold surface, cannot be detected in grazing angle FTIR, the ratio between the intensities of the amide-I band (1,663 cm^{-1}) and amide-II band (1,549 cm^{-1}) indicates to what extend the molecules in the monolayer are oriented perpendicular to the gold surface.[48,49] Based on the FTIR spectra it was possible to calculate the tilt angle, namely the angle between the molecular axis and the surface normal.

The PM-IRRAS spectra is shown in Figure 12. The orientation of the peptide molecules immobilized on the gold surface was determined using the following equation: $\frac{I_1}{I_2} = 1.5 \times \frac{(3cos^2\gamma-1)(3\cos^2\theta_1-1)+2}{(3cos^2\gamma-1)(3\cos^2\theta_2-1)+2}$, where I_1 and I_2 are the absorbance of amide I and amide II bands, respectively, γ is the tilt angle of the helical axis with respect to the surface normal, and $\theta_{1,2}$ are the angles between the transition moment and the helix axis. The values of θ_1 and θ_2 were set to 39° and 75°, respectively.[49] The value of the tilt angle γ of the helix with respect to the surface normal was found to be $\gamma = 46°$.

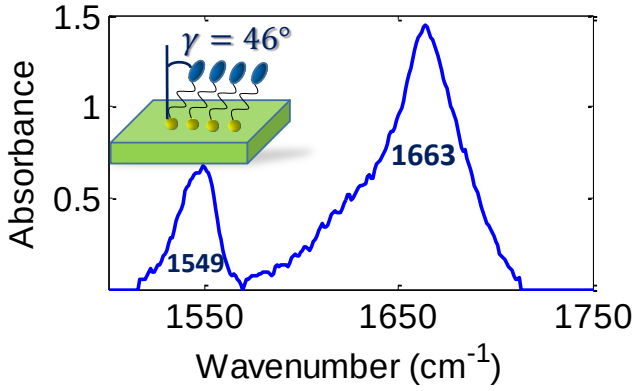

Figure 12: PM-IRRAS spectra of poly L-alanine monolayer on a gold surface. The frequencies of amide-I and amide-II vibrations indicate that the monolayer is in a helix form, their ratio gives information about the tilt angle of the molecules adsorption relatively to the surface normal.

3.2.2 AFM measurements

The thickness of the chiral monolayer was characterized by atomic force microscopy (Figure 13). In this case, an area of about $400\,nm^2$ was removed by scratching the molecules from the surface (see inset). The uncovered area shows a depth of about $\delta = 3.0\,nm$ relative to the unscratched area.

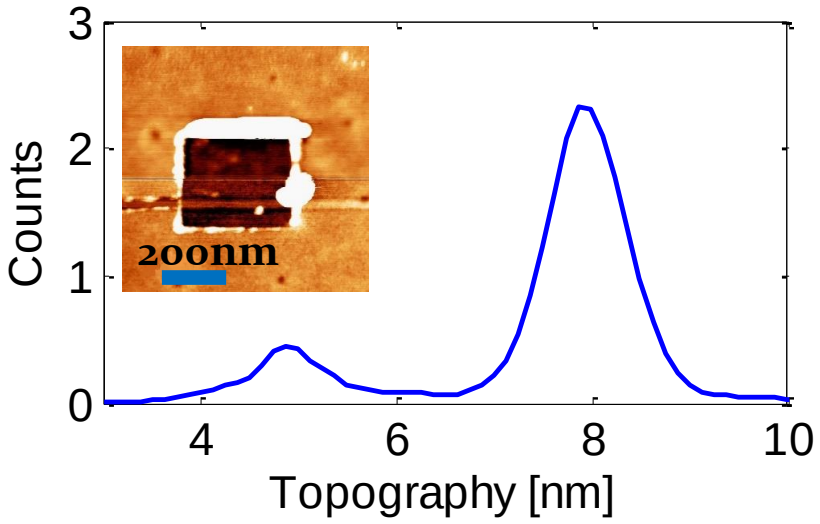

Figure 13 –AFM image of the chiral monolayer that was scratched in the middle (inset). From the HEIGHT data the histogram was built by which the heights of surface and scratched area were determined. The layer estimated thickness is **3 *nm***.

Taking into account both PM-IRRAS and AFM measurements, with simple trigonometry: $\cos(\gamma) = \delta/h_{mol}$, we calculate the chiral monolayer length to be $h_{mol} = 4.3\,nm$.

3.2.3 NCs characterization

The 610 nm CdSe NCs absorption spectrum was characterized by illumination with a deuterium/halogen light source (Avantes Avalight-DH-S-BAL) and then measurement of the light transmission with a visible-NIR spectrometer (Ocean Optics USB4000). The emission was measured separately while illuminating the solution with a 532nm laser. Both spectrums are shown in Figure 14 and represent a spectral behavior of the NCs with main emission peak at $610\ nm/$

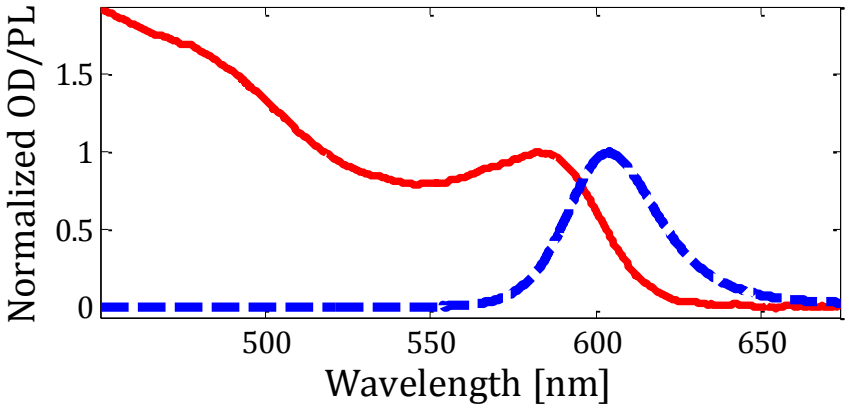

Figure 14: Absorption and emission spectra of 610 nm CdSe QDs in a cuvette, showing absorption of wavelengths lower than 610 nm followed by emission centered on the 610 nm wavelength.

After adsorption of the NCs as a monolayer on top of the molecules, the sample was examined in the scanning electron microscope (SEM). The resulting scan, shown in Figure 15, indicates a good adsorption of the CdSe NCs on top of the α helix monolayer, covering homogeneously the surface of the gold substrate.

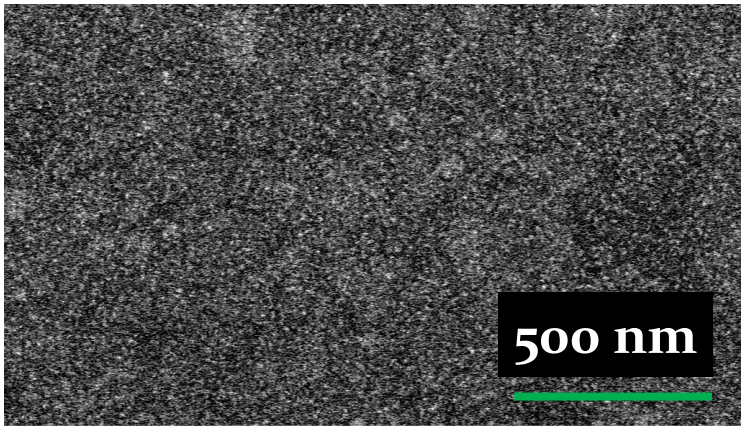

Figure 15 – SEM image of CdSe QDs with the bandgap of 610 nm, adsorbed on the top of a monolayer of chiral molecules.

3.3 Sample preparation process

3.3.1 Sample preparation pre-adsorption

A substrate of Si (100) wafer was treated thermally to produce an approximate 1μm SiO_2 layer. Standard optical lithography was applied in order to create the contacts patterning (Elaborated in Appendix A). Thin adhesion layers of 15nm Ti followed by 150nm Au for contacts are evaporated. The sample then went through a liftoff process, washed with 2-Propanol and dried with a flow of Nitrogen. In order to create an insulation layer, 150nm of Al_2O_3 is evaporated while the rotating stage holding the samples is slightly (10°) tilted in order to create a homogenous layer on the whole sample. An additional optical lithography process exposes holes in the photoresist layer above the adsorption areas, gold contacts. Afterwards the sample undergoes a wet etch process using buffer HF for 1:30 minutes. Before wafer dicing, a protective resist is placed on top of the wafer, later on the wafer is diced as a 7.5mm by 7.5mm samples' matrix (See appendix A for additional information).

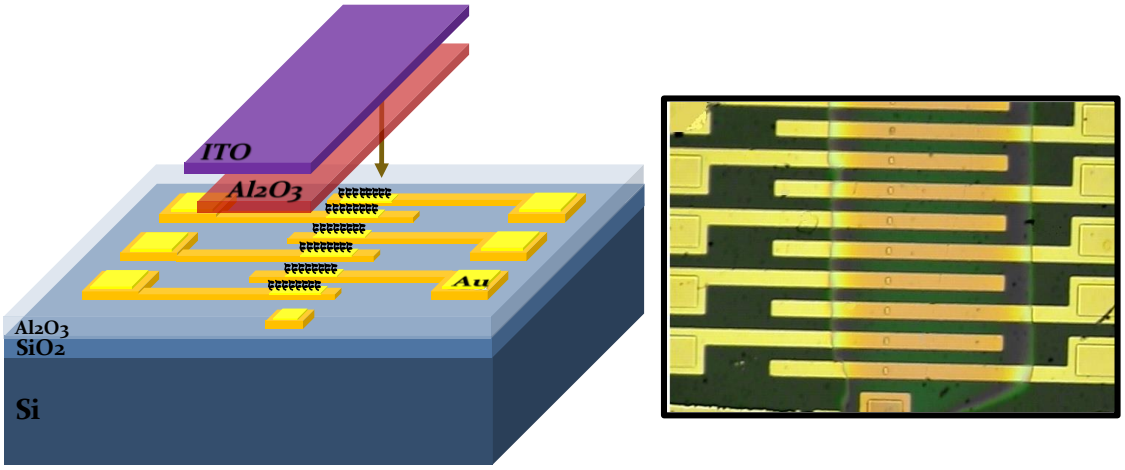

Figure 16: A schematic drawing and photo of the sample used in the measurements. Several contacts were fabricated in order to achieve better statistics. a. A schematic description of the sample design. b. A microscope image of a sample past fabrication process. The Adsorption areas are visible in the middle of the contacts, covered by the upper ITO layer.

3.3.2 Molecules and NCs preparation

α Helix Polyalanine-L (36 amino acids) was synthesized by Sigma-Aldrich Co. LLC. according to our requirements.[46] The molecules have a head terminal of Carboxylic Acid (-COOH) to facilitate covalent bonds to oxide surfaces (Aluminum, Titanium etc.) while the tail terminal has Amine (NH3) and Thiol (Sulfur hydride –Cysteine amino acid) groups that attach covalently to Gold. The α Helix Polyalanine was dissolved in Ethanol to a 1mM concentration.

For reference measurements 1,9-nonanedithiol (9DT) non-chiral molecules were used, purchased from Sigma-Aldrich Co. LLC. The $9DT$ solution was further diluted in Ethanol to a 1mM concentration.

The NCs used in the research are core CdSe NCs with main emission peaks at $610\,nm$ and $520\,nm$ purchased from Sigma-Aldrich Co. LLC. The NC solution was further diluted in toluene solvent to the concentration of $0.5\,\frac{mg}{ml}$.

3.3.3 Sample preparation post-adsorption

Freshly prepared samples were then taken to evaporation of 4-5nm Al2O3 through a metal mask, performed with stage temperature of $-5°C$ in order to avoid damage to the adsorbed layers. An additional layer of 2nm Al2O3 was then evaporated at room temperature in order to seal pinholes that are usually created in the Al_2O_3. This Al_2O_3 layer acts as a tunnel barrier, and prevents the upper contact from short-circuiting the lower contact. Afterwards, a 150nm layer of Indium Titanium Oxide (ITO) was sputtered through the same mask. This layer is the transparent upper contact of the sample. The full device was then mounted and wire bonded (Kulicke@Soffa Ball Bonder 4522) to a 44 header chip that is compatible for our measurements.

4 Results and Discussion

4.1 Chiral molecules and 610 nm CdSe NCs

The hybrid device with the layer of CdSe (emission wavelength 610 mn) on top of α helix chiral molecules was designated to test different electric responses when illuminated with circularly polarized light. As described previously in chapter 2.1.1.2, circularly polarized light excitation of NCs creates electron-hole pairs with the spin states of $(S_e, S_h)_{+1/2,+3/2}$ or $(S_e, S_h)_{-1/2,-3/2}$, depending on the handedness of the light polarization.

By selectively controlling the electron-hole spin states with different circularly polarized light we affect the probability of the charge transfer through the chiral monolayer. This is due to the CISS effect where the probability is dependent on the charge sign as well as on the favored spin state, as seen in chapter 2.1.1.1. Therefore for a given bias voltage on the device we expect a higher current for a selected circular polarization than the counter circular polarization. Furthermore, this trend is expected to flip once the bias voltage is reversed, giving rise to antisymmetric I-V curves for negative and positive biases. This effect is schematically portrayed in Figure 17, where the device is under illumination of right circular polarized light, and a reverse bias is applied.

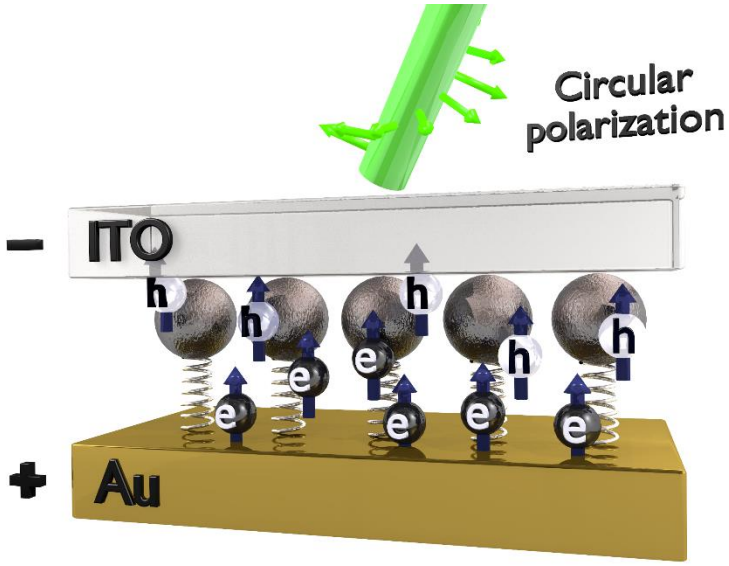

Figure 17: Schematic representation of the charge separation in the device. Electron-hole pairs are created when exciting with a 532 nm wavelength laser. The angular momentum of light is transferred to the charges' spins. Right circular polarization creates charges with spin pointing up. Charges carrying the favored spin, electrons in this illustration, are transferred easily through the chiral monolayer when a reverse voltage bias is applied.

In Figure 17, the light creates electron-hole pairs with spin facing up. The bias drives the electrons downwards through the chiral molecules and the holes to the upper *ITO* contact. The spin and charge values of the electrons are favored by the CISS effect, therefore the current is higher than for electrons with spin down (left polarization) or holes with spin up (forward bias). For the opposite bias that drives the holes through the chiral monolayer, the left circular polarized light will create holes with spins facing down, which are favored by the CISS effect.

This effect can be modeled to a pseudo CISS gap energy diagram, described in Figure 18. In this model, the gap changes for different circular polarizations, enabling charge separation.

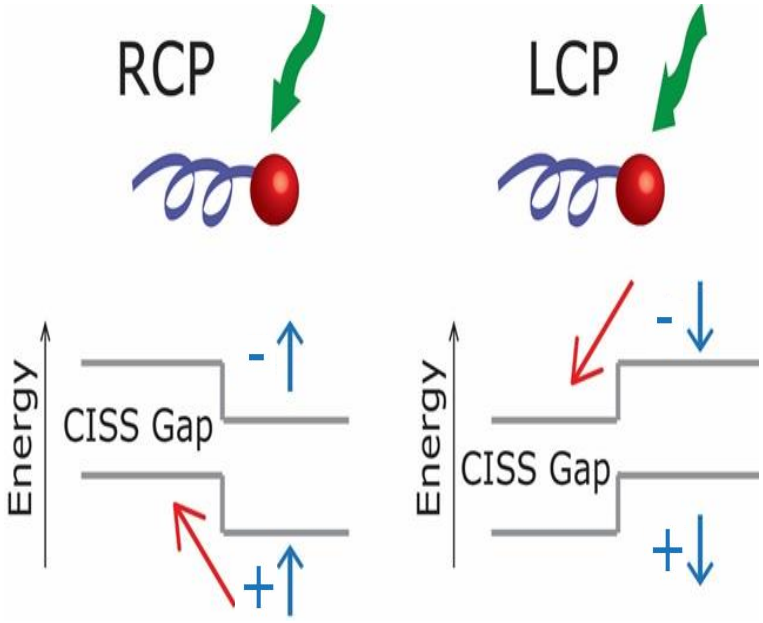

Figure 18: A general energetic perspective model, in which there is a pseudo CISS gap that changes according to the exciton polarization on the NCs. Charges carrying the favored spin, will have energetic preference to transfer through the chiral monolayer.

The expected I-V curve is portrayed in Figure 19, with anti-symmetrical properties for different light polarization and bias sign.

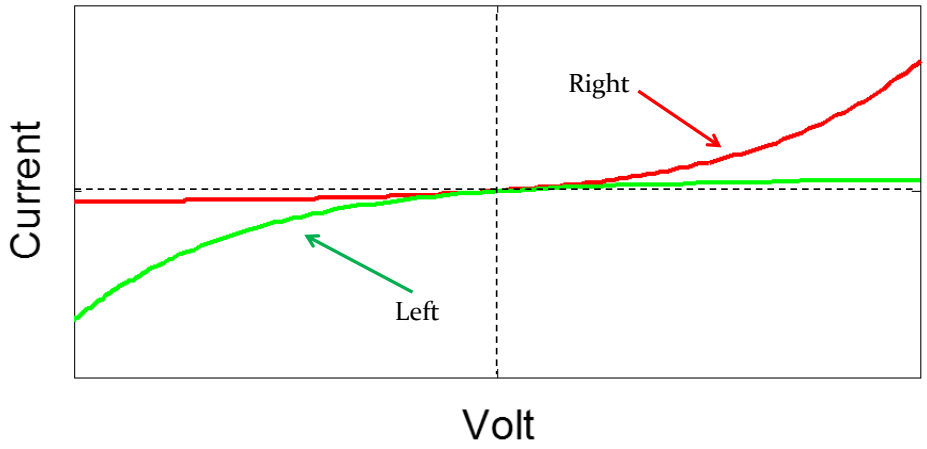

Figure 19: Schematic I-V curve expected for different polarizations. The anti-symmetry is attributed to the CISS effect and its dependence on the charge and spin sign. Therefore, for opposite biases, different charges will be driven through the chiral monolayer, and for opposite circular polarizations, the charges will have different spin signs – affecting the probability of transferring through the chiral monolayer.

4.1.1 I-V measurements of a device with chiral molecules

The I-V measurements were taken on a device with chiral molecules and CdSe with the emission gap of 610nm. Input bias voltages were given between -1.5V to 1.5V, and the current was measured. Resulting I-V plots demonstrate different illuminations of right (red), left (green) and linearly (blue) polarized light, as seen in Figure 20.

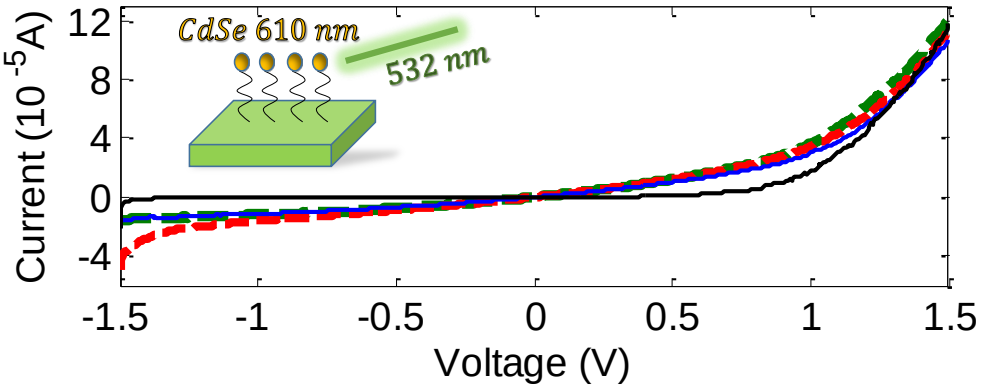

Figure 20: I-V curve of a device with adsorbed CdSe QDS with the bandgap of 610 *nm* on top of chiral molecules, under polarized light illumination. The I–V curves for the three polarizations (Red– right, Blue – linear, Green – left) illuminated, show distinct current responses responding well above the dark current (black)

The device with chiral molecules and NCs has a diode-like shaped feature resulting from the Au-NCs–ITO interface in the device. Upon illumination with different light polarizations the current response was measured. This response is governed by both coherent spin relaxation processes and fast non coherent processes. It is seen that the response upon illumination is greater than the dark current for forward and reverse biases. Furthermore, there is a response difference between the different polarizations. In order to retain solely the polarization dependence for the current response, we subtract the linear polarization response from the left and right circular polarization (Figure 21).

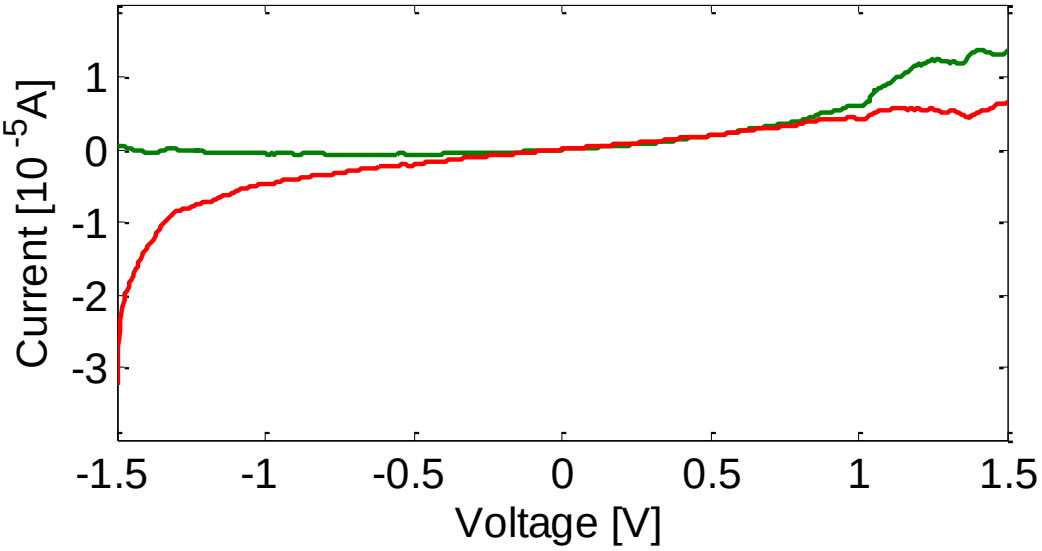

Figure 21: Left (green) and right (red) polarization current responses after the linear current was subtracted from them. The right polarization creates electrons with favored spins, which are driven with less resistance through the chiral molecules for reversed voltage bias. On the other hand, the holes don't have the required spin value, therefor in forward bias the left polarization has a stronger response.

The circularly right polarized light creates electrons with favored spins according to the CISS effect, which are driven through the chiral molecules once a reverse voltage bias is applied. On the other hand, the holes don't have the required spin value, therefore in forward bias the left polarization has a stronger response while in reverse bias the right circular polarization response is stronger.

4.1.2 Energetic gap between the CISS spin states

Improving the Al_2O_3 tunnel barrier allowed the usage of higher bias voltages. Nevertheless, our measuring voltage was limited by the stability of the molecules monolayer. This allowed us to extend the voltages used up to 2.5 Volts. The difference between polarizations, resulted by the CISS effect and determined by different electron spin states was overcome once higher voltages were applied in reverse bias, as seen in Figure 22 . This can be explained due to the strength of the spin-orbit coupling (SOC) of the charge passing through a chiral monolayer with the chiral potential [28,50]. It was discussed in chapter 2.1.1.2 that SOC creates an energetic difference of spin states of the charges transferring through a chiral monolayer. This energetic difference was measured in previous studies of double stranded DNA oligomers to be of 0.5 eV [28], taking twice the value to be the energy gap between two different spin states. In Figure 22 we observe that the difference between the polarizations is diminished at around 2 volts.

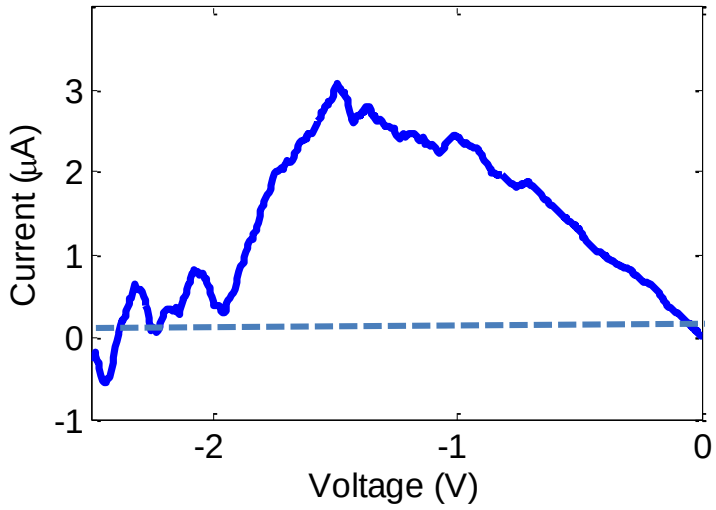

Figure 22: Response difference between left and right circular polarizations with bias extended to -2.5 V. The current difference between polarizations diminishes when the bias voltage reaches about 2 Volts, possibly due to gap overcoming.

4.1.3 Changing light flux under constant bias

Another way to measure the different current responses to different polarized illuminations was to have a constant reverse bias voltage of $-1.5\,Volts$ and illuminate the device with tuned light power levels. The results are displayed in Figure 23. The current response grows stronger with increasing light power for all polarizations. This occurs since stronger light power excites more charges in the NCs per second, which under bias enables a stronger current to pass through the device. The different response between the polarizations is of major significance. The left circular polarization has the weakest current response similarly to the previous I-V measurement under reverse bias. Right circular polarization has the strongest current and the linear polarization is in between. It is important to notice that the CISS response does not grow linearly with the intensity as at high light power, Auger process that does not conserve spin becomes dominant. As expected, the linear response is somewhat between the left and right circular polarization response. This agrees with the understanding that linear polarization holds equal components of left and right polarizations, thus creating also equal amount of opposite spin carriers in the NCs. Therefore we should expect that the linear response would be the sum of the responses of both circular polarizations at half the intensity. This is not exactly the case and the difference could be ascribed to the non-linearity of the spin T2 decay at different intensities and polarizations.[51]

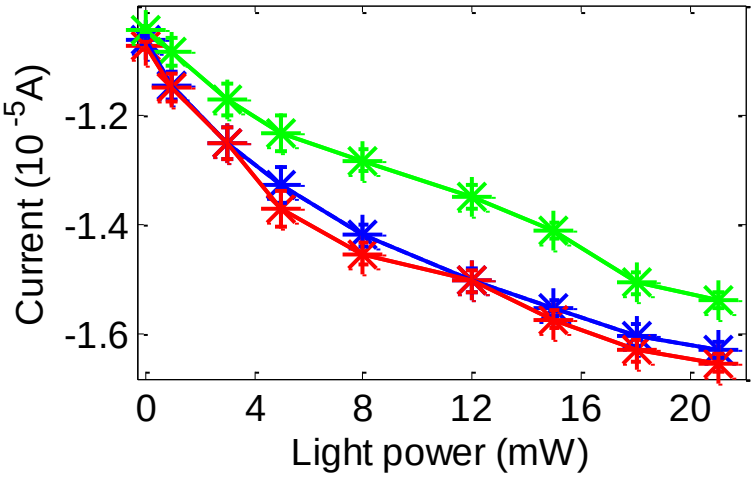

Figure 23: Current responses of different polarizations (Red – right, Blue – linear, Green – left) at changing light powers, for a constant bias of -1.5 Volts.

4.2 Control measurements

To be certain the results we have are due to the CISS effect and choice of NCs, and not because of other effects – such as surface plasmonic excitations in the gold substrate or different spin-orbit couplings not attributed to the CISS effect, we performed a series of control measurements. These different measurements required changes made in the device fabrication, such as using a non-chiral monolayer of 1,9-nonanedithiol (9DT) instead of α helix chiral molecules, using different NCs, removing the NCs from the device, and lastly exciting the sample at different laser wavelength. These changes resulted in different circuit resistances leading to different circuit I-V characteristics, and therefore couldn't be directly compared to the previous results. Therefor two methods of data analysis were introduced. In order to compare the response of the device to light, the absolute response of the devices was calculated using the formula: $A.R = \left|\frac{I_{light}-I_{dark}}{I_{dark}}\right| * 100$, which enabled the comparison between the different measurements. The absolute response of the different devices under different circular polarization illuminations is presented in Figure 24.

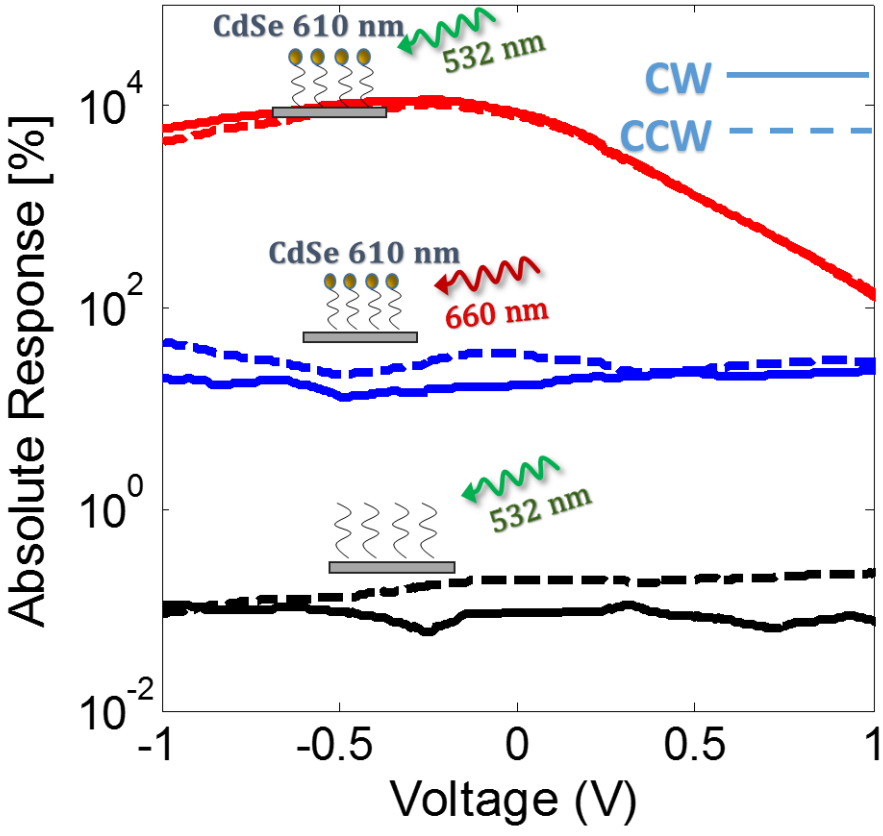

Figure 24 – Absolute response of three samples, comparing the CW and CCW response to dark current response and giving information whether the devices reacts to the illuminations. As seen the device with chiral molecules and NCs, illuminated above bandgap has a response two orders of magnitudes larger than a device with below band gap illumination, and four order of magnitude larger than a device without NPs.

The absolute response for device with chiral molecules and CdSe NCs is seen in Figure 24. The red curve represent the response when the system is excited with energies above the energy bang gap of the NCs (532 nm laser). A clear large response to the illumination is measured for both polarizations, which agrees with the previous curves we presented in Figure 20. When exiting below the energy band gap (blue) or a system without the NCs (black) the response is small.

4.2.1 The NCs response

Charges and current under illumination can be created by different mechanisms. These mechanisms may not be related to the NCs. For example illumination on a gold substrate can create surface plasmons in the visible wavelengths which can change the Schottky barrier properties.[52] In order to validate that the charges were generated in the CdSe NCs we performed a couple of control measurements.

First, we measured the absolute response when exciting with below-bandgap illumination (Figure 24 blue). Exciting at 660 *nm*, which is well below the bandgap of the average size CdSe NCs used (as seen in Figure 14), the absolute response is two orders of magnitude smaller than the response measured for above bandgap illumination seen in red.

An additional way to ensure that the response is not attributed to other effects was to fabricate a device without the NCs layer on top of the chiral molecules. The absolute response of the device, shown in Figure 24 in black, is weaker than below bandgap illumination, four orders of magnitude weaker than the response of the original device. Thus we can conclude that the previous measurements are mainly attributed to charges created in the NCs.

4.2.2 Non-chiral molecules

The charge separation effect is expected to disappear once we use non-chiral molecules to link the NCs to the gold surface. Control measurements were performed separately on devices fabricated with the adsorption of non-chiral molecules, 1,9-nonanedithiol (9DT), followed by adsorption of CdSe NCs (610 *nm*).

In order to be able to compare between different devices we normalized the current responses of the circular polarizations with the linear current response using the following equation: $Asymmetry = \frac{I_{circular} - I_{linear}}{I_{linear}} * 100$. This allowed us to follow the circular polarization illumination responses on the system. The plots for different devices are seen in Figure 25.

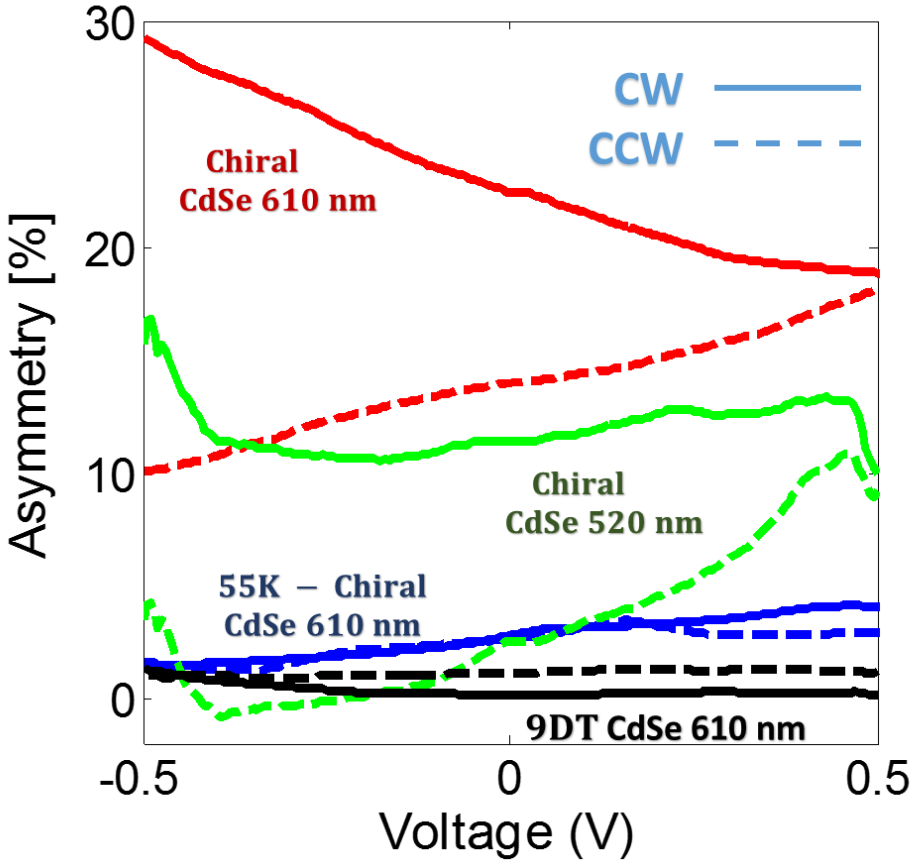

Figure 25: Asymmetry between the circular polarizations normalized to the linear response, for four different devices. For the device with chiral molecules and 610 nm CdSe NPs a distinct asymmetry is seen between CW and CCW illuminations, especially in the negative bias, thus showing spin coherence influence on charge separation. This is seen less for smaller NPs which are known to have an electron spin flip, affecting the coherence of the states. For a cooled down system and reference non-chiral 9DT molecules the asymmetry is much lower indicating no CISS effect in the device.

The asymmetry measurements allowed us to compare the influence of the chirality of the molecules on the performance of the devices. For the device with chiral molecules and 610 nm CdSe NPs a distinct asymmetry is seen between CW and CCW illuminations, especially in the negative bias. The difference disappears and flips for positive biases, which agrees with Figure 21, where the CCW polarization becomes

stronger in positive biases, thus showing spin coherence influence on charge separation.

Asymmetry curves for devices fabricated with the adsorption of non-chiral molecules, 1,9-nonanedithiol (9DT), followed by adsorption of CdSe QDs (610 nm), seen in Figure 25 in black, show no significant difference between CCW and CW polarizations over the linear polarization. This indicates no CISS effect when non-chiral molecules are used.

4.3 Further measurements under different conditions and device structures

To provide us a better understanding of the effect and its boundaries, we performed several measurements by changing the temperature and the NCs size, and measuring the response of the device to light under zero bias by measuring the asymmetry response.

4.3.1 Smaller CdSe NCs

As described in the previous chapter 2.2.1, the CdSe NCs emission gap is dependent on its size. Choosing smaller sized NCs will create a larger bandgap, allowing us to use CdSe NCs with the main emission peak at 520 nm. These NCs were chosen to enable selective excitation of a narrow size-ensemble of NCs that overlaps with the laser's wavelength. [44] Exciting at the band gap could reduce phononic spin relaxation decoherence effects. Better spin coherence would increase the spin lifetimes, thus increasing the effectivity of the CISS effect on the charges transferred through the chiral monolayer. Thus in the simple case we should expect an increase in the charge separation process. On the other hand, in previous studies of smaller CdSe NCs (with the absorption peak of 498 nm and 578 nm) an electron spin state flip was measured.[44] This compromises the charge separation process in our device configuration.

In Figure 25 the asymmetry curves are seen in green, showing a smaller spin dependent charge separation effect than for larger NPs. Thus the measurements seem to be sensitive to the spin coherent time of the dots and to the electron spin flip, which in the case of smaller CdSe NCs becomes more dominant and compromises the charge separation effect.

4.3.2 Cooling down

Taking into account the excited states life time, cooling the system down could lengthen spin coherence and excited states life times. In CdSe NCs, the exciton life time is ~1 ns at room temperature and ~400 ns at 1°K.[53] Similar trends also happen for the spin dephasing time. At room temperature the transverse spin relaxation time T_2^* was measured to be $T_2^* = 136 \pm 2\ ps$ and at 1.6°K T_2^*~5 ns.[54,55] A longer exciton life time means there is more probability for the charges to be transferred through the chiral molecules rather than recombining. Longer spin coherence times, like described before could increase the efficiency of the charge separation process. On the other hand, it has been shown that below 150K the chiral molecules used in this study undergo structural phase transition, thus rendering a weak spin selectivity CISS effect.[56,57] In order to test the two competing effects, we measured the device with adsorbed chiral molecules and extracted the asymmetry curves for different circular polarizations at the temperature of 55° K, seen in Figure 25 in blue. These results show a weak charge separation, with similar asymmetry for both circular polarizations, indicating that the CISS effect is less prominent at low temperatures.

4.3.3 Measuring response of illumination under zero bias

Using a nano voltmeter we measured the voltage response of the device under illumination of different polarizations. We wanted to see if there's a difference between the polarizations when the device is not biased by outside voltage difference. The voltage measurements for different polarized illuminations are presented in Figure 26. It is possible to see that the device responds equally to all polarization illuminations. When illuminated, the light excites the NCs in the device, creating electron-hole pairs. Due to the electrostatic interaction between the electrons and holes, an electric field is created and voltage step is built in the device, which is then measured. Because there is no bias, the charges do not transfer through the chiral monolayer and therefore the CISS effect is not effective in this case.

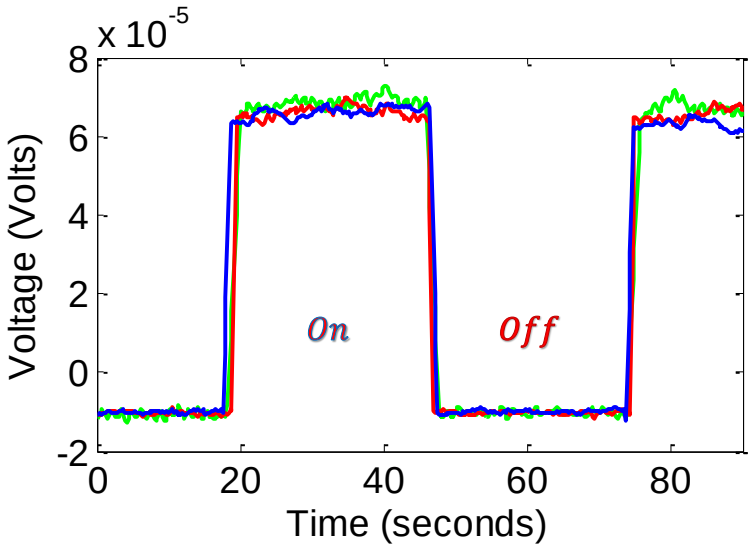

Figure 26: Voltage response measurements as a function of on\off illumination at all polarizations (red – right, green – left, blue – linear). No difference was measured for the different polarizations.

5 Summery

In the work presented here, we have demonstrated nano scale charge separation using a thin layer device based on chiral molecules and semiconductor NCs. We have shown that the device was sensitive to the circular polarization excitation of the NCs, measuring a significant difference in the current responses in our device, which was attributed to the CISS effect and to room temperature charge separation. Our measurements were susceptible to the spin states dynamics (electron and hole spin flip times) of the excitons created in the NCs, which are dependent on the size of the QDs used. Finally, we performed control measurements of non-chiral 9DT molecules in order to show the effect is solely attributed to the CISS effect.

In the future, the devices could be fabricated with nano sized features. A possible future application could be the development of charge separating inks, paints or sheets.

In the next section (see also paper in Appendix C) we utilized chiral nanocellulose and NCs to reinforce and functionalize a biodegradable transparent film to create a transparent, strong and optically tunable plastic film. In the future we could incorporate these properties to create charge films that creates charge separation from solar energy.

6 Nano Crystalline Cellulose optically tunable films

Another research work performed in collaboration with Oded Shoseyov's group from the plant sciences department was to utilize strong, optically controlled, biodegradable films made of nano crystalline cellulose (NCC) combine with NCs. These films have the potential for many applications such as green houses and food packaging.

NCC, produced by hydrolysis of cellulose fibers has attracted a lot of attention due to its physical, chemical and mechanical properties. A variety of cellulose sources can be used in order to produce NCC, such as cotton,[58] wood,[59] bacterial cellulose,[60,61] microcrystalline cellulose (MCC),[62] and even recycled wood pulp, which is present in waste streams of paper mills and municipal sewage system sludge. The use of sulfuric acid in the hydrolysis process results in rod-shaped nanoparticles, which are negatively charged due to the formation of sulphate ester groups on their surface, leading to a well dispersed and stable water suspension. Above a certain critical concentration, the NCC suspension can form ordered liquid crystal phases.[63] The advantages of NCC, namely its superb properties, renewability, biodegradability and abundance, lead to its recognition as one of the most promising materials for future applications. NCC is nearly as strong as Kevlar and can be added to materials to increase their strength and stiffness.[64–67] Many studies in recent years have shown that NCC can be used as a building block in a variety of applications. The most common use of NCC is as filler in nanocomposite materials[68–70] but it has also been utilized in other applications such as adhesives,[71,72] foams, aerogels [73,74] and films [75–77]. Upon drying, NCC liquid crystal water suspension is known to self-assemble into macro scale ordered films, as seen in Figure 27 a and b.

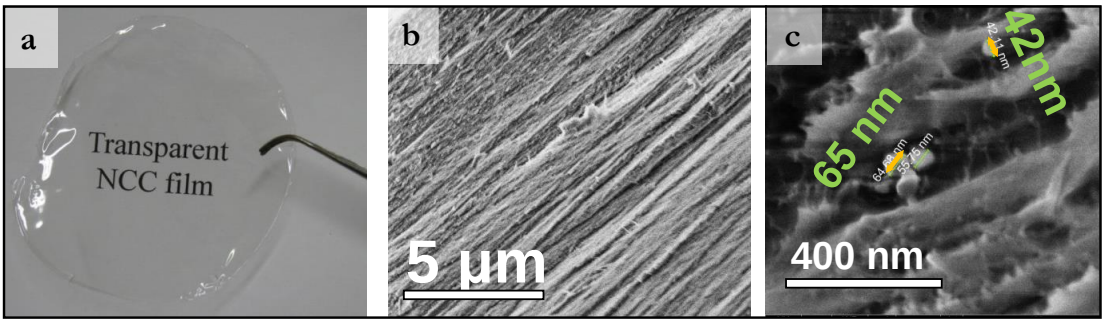

Figure 27: (a) Dried NCC film. (b) SEM micrograph of an independent NCC film prepared with ZnO NCs. (c) Zoomed SEM micrograph of an independent NCC film prepared with ZnO NCs. note the ZnO NCs located between the layered films.

NCC films can be transparent or semi translucent and can retain the liquid crystalline order of the suspension.[78] Furthermore, NCC-based films and composite material were found to have good gas barrier properties, attributed mainly to the high crystallinity of the nano crystals which lower the diffusion of gas molecules and elongate the path they travel through the film.[79] Alone or combined with other materials, self-assembled NCC films with intriguing properties enable cost effective, tunable coatings for large surfaces.

In the study we have combined the NCC properties with the NCs to fabricate strong, optically controlled, biodegradable films that have the potential for many applications such as green houses and food packaging. We have used thin self-assembled layers of NCC to trap NCs inside the NCC films. The NCs can be well dispersed within NCC films, as seen in fig. 1c. For both greenhouses and packaging applications the optical tunability of the absorption spectrum as well as mechanical reinforcement and gas barrier properties are needed. For food packaging it is critical to prevent UV light transmission in order to prevent the peptides denaturation[80] and photo oxidation of essential oils.[81] In greenhouses UV can reduce insect parasites navigation capabilities [82] and infrared absorption enhances the efficiency of the greenhouse.[83,84]

In the results, see appendix C, we showed we could utilize ZnO NCs to absorb the UV range, and SiO_2 NCs to absorb light in the IR range. We also used core-shell CdSe/ZnS NCs that absorb light in the UV and emit light in the visible spectrum. All of these results didn't affect the transparency of the films in the visible range.

7 Future Work

7.1 improving the device

- *Different tunneling barriers*: During my research the main bottleneck for most experiments was the thin Al_2O_3 insulating layer on top of the monolayer. Further research is required in order to find the precise process for the deposition of the Al_2O_3 layer. Another solution can be the Atomic Layer Deposition (ALD), which creates a very thin insulating layer (angstrom scale) that would enable larger responses with less resistance. Although ALD requires high temperatures (higher than 600C) that might cause damage to the organic layer, it is still possible to lower the temperature or to use other molecules that would withstand such temperatures. In addition, conducting polymers might be available in the near future. In that case the tunneling will only be conducted through the monolayer resulting in a substantial resistance decrease.

- *Using a different metal for the Lower contact*: Taking in account the energetic diagram of the interface of $Au - CdSe - ITO$, we can draw a schematic picture of the energy levels with the known values of working functions of metals,[85–87] and of the electron affinity of CdSe NCs, [88] seen in Figure 28. Since $E_{f_{CdSe}}$ is lower than than $E_{f_{Au}}$, there'll be an energetic gap for electrons transferring from the NCs to the lower contact. Replacing the lower contact to evaporated Pt with $E_{f_{Pt}} > E_{f_{CdSe}}$ will allow easier transfer of electrons to the lower contact, enabling better charge separation, perhaps also at zero bias.

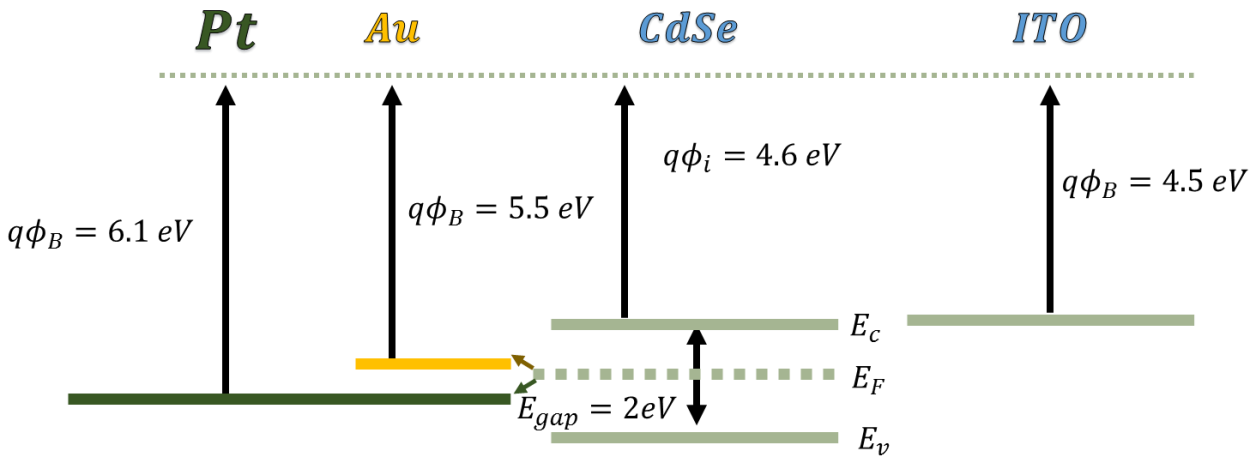

Figure 28: Energetic scheme of the interface between the lower and upper contact with the NCS (***Au – CdSe – ITO***), and with ***Pt*** replacing the ***Au*** as a lower contact.

- Using longer molecules with more amino acids – previous studies showed that the spin polarization effect increases monotonically with the length of the chiral molecules.[28] Using longer molecules will enable us to create better charge separation, and we would expect the asymmetry measurements, seen in Figure 25, to grow and show distinct difference between CW and CCW circular polarizations.

7.2 Multilayered charge separation device

Another possibility of improving the charge separation efficiency is to fabricate devices with further adsorption of more layers. A suggestion for such a device is depicted in Figure 29 – The first layer is similar to the device fabricated in this work. The second layer has opposite handed chiral molecules followed by another adsorption of CdSe NCs and ITO contact – which is connected to the lower contact. Further layers can be adsorbed then with alternating handedness, with contacts connected to each other also in an alternating manner. This configuration can increase the charge separation efficiency, since a monolayer of NCs absorb about 2% of light[89], several layers could increase absorbance therefore also charge separation efficiency. All charges created will be separated by the CISS effect through the chiral molecules.

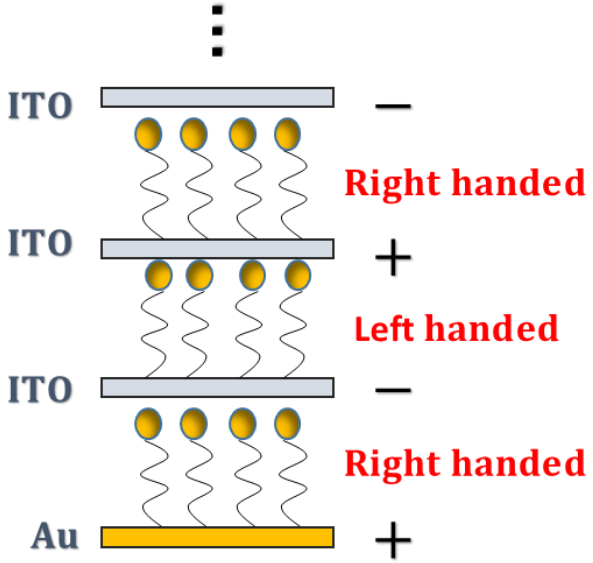

Figure 29: A sketch for a multilayered device, consisted of adsorption of both right and left handed chiral molecules.

7.3 Combine charge separation in NCC sheets

As shown is chapter 6, in a previous work we incorporated NCs with nano crystalline cellulose (NCC) to fabricate strong, optically controlled, biodegradable films that have the potential for many applications such as green houses and food packaging. A future work could be to combine chiral molecules with transparent contacts in NCC films to create thin active, charge separating coatings or smart sheets.

Appendix A: Elaboration on the Sample preparation processes

Gold contacts optical lithography – Oxidized (1um) Si (100) wafer was placed into a vertical stand and undergoes 3 minutes of sonication in Acetone, then 3 minutes of sonication in Methanol, 3 minutes of sonication in 2-Propanol. Afterwards the wafer is dried using a flow of Nitrogen.

The wafer was attached with vacuum to a hot plate heated to 120°C for 5 minutes, in order to remove any humid contaminants, followed by Nitrogen cooling. Then the wafer was placed on a spin coater (Suss delta 6RC) and coated with nLOF2020 negative photo resist (AZ Electronic Materials). The following parameters of the spinner are used: 3/3/600 → 40/4/4000 (Seconds/Ramp/RPM accordingly). The wafer was taken to a hot plate bake in 110°C with vacuum attachment for 75 seconds and cooled by Nitrogen.

Next the wafer is placed on the Mask aligner (Suss MA06) stage while being held with vacuum. The following parameters are entered into the MA: soft contact and dose of $37.5 mJ/cm^2$ and $63 mJ/cm^2$ were applied. Once the lithography process is finished, the wafer was heated to 110°C for 75 seconds on hot plate and cooled by Nitrogen.

Lastly the sample was developed using AZ726 developer (AZ Electronic Materials) for 70 seconds while being shaken. During this procedure the patterning on the wafer should become visible. Afterwards the sample was washed and shaken inside distilled water and dried under a flow of Nitrogen.

Gold contacts evaporation – Titanium and Gold evaporation was performed in the thin film deposition system (VST TFDS-141E). The evaporation process was carried out under a pressure of $10^{-7}\ Torr$, while the stage is cooled to -5°C and the deposition rate is 0.5nm/sec.

Gold contacts exposure in Al_2O_3 lithography process - Using a vertical stand the sample undergoes 3 minutes of sonication in Acetone, then 3 minutes of sonication in Methanol, 3 minutes of sonication in 2-Propanol. Afterwards the sample was dried using a flow of Nitrogen.

Cleaning before evaporation was done by a hot plate at 120°C for 5 minutes, in order to remove any humid contaminants, followed by Nitrogen cooling. The sample was then placed in a spin coater (Suss delta 6RC) and coated with AZ1505 positive photo resist (AZ Electronic Materials). Spinner was used with the following parameters: 2/2/600 → 30/3/4000 (Seconds/Ramp/RPM accordingly). Then is the sample was vacuum placed for a hot plate bake at 110°C for 90 seconds and cooled by Nitrogen.

Mask aligner (Suss MA06) was used for lithography. The following parameters are entered into the MA06: soft contact and dose of $22.5 mJ/cm^2$ and $37.8 mJ/cm^2$. Developing was done by AZ726 developer (AZ Electronic Materials) for 35 seconds while being shaken. During this procedure the patterning on the wafer should become visible. Lastly the sample was washed and shaken inside distilled water and dried under a flow of Nitrogen.

<u>Al_2O_3 etching process</u> – Prior to etching the sample was hard baked on a 120°C hot plate attached with vacuum and then cooled with Nitrogen. A Buffer Oxided HF (BHF) 7:1 solution was used, with an approximate etch rate of 50nm/min (a preliminary test should be conducted on a different wafer in order to establish the correct etch time). The sample was taken out directly from the BHF and placed in distilled water.

<u>Sample Dicing</u> – Prior to dicing, the sample was cleaned with Acetone and 2-Propanol and then is placed in the spinner. Then the sample was coated with a S1813 protective photoresist. Spinner was used with the following parameters: 2/2/600 → 30/3/4000 (Seconds/Ramp/RPM accordingly). The resist was baked on a hot plate in 110°C for 100 seconds and then cooled by Nitrogen. A dicer (ADT 7100 2" Pro Vectus) diced the sample as 7.5mm by 7.5mm matrix elements with a 40um cutting saw.

Appendix B: Submitted paper –

Nano Scale Charge separation using Chiral Molecules

N. Peer[a], *I. Dujovne*[a,b], *S. Yochelis*[a] *and Y. Paltiel*[a]*

[a] Department of Applied Physics, The Hebrew University of Jerusalem, Givat Ram, Jerusalem 9190401, Israel

[b] Department of Physics, University of Massachusetts, Amherst, MA 01003, USA

KEYWORDS Chiral molecules, charge separation, spin, polarization, excitons, CISS,

ABSTRACT

Charge separation is a fundamental process currently being used in a large variety of devices. Typically charge separation requires doped P/N junctions that, at the nano scale, are difficult to form due to the small number of participating atoms. Thus it is not trivial to separate charges at the nanometric scale in a simple flexible way. Recently, studies of electron transfer through organic helical chiral molecules have shown that electron transmission through these molecules is spin dependent at ambient temperatures. Utilizing semiconductor nanocrystals and helical chiral molecules, we created a room-temperature optically activated, thin-layer, charge-separating nanoscale device. Total efficiency of separation is sensitive to the polarization of the light. The fabrication process is simple and uses self-assembly methods that could be applied to a wide variety of nano crystals based devices. From the fundamental point of view the induced chiral

charge separation may be relevant for physical and biological processes such as charge separation in photosynthesis.

[Introduction]

Charge separation is essential for large variety of optoelectronic devices, such as solar cells and photodetectors.[1] A subset of these devices are photovoltaic devices, that are charge-separating systems operating by light energy.[2] Nowadays, these systems are mainly based on doped silicon, in which a junction is formed between a donor dopant (p-type) and an acceptor dopant (n-type). Charge diffusion equalizes the Fermi energy of both layers creating an electric field called the "depletion region" that has a built in potential. Under an applied bias voltage and above bandgap illumination, the device will create an electron-hole pair that will be separated according to the built-in potential. One of the main drawbacks in these devices arises when miniaturization is required, since the amount of doping in a semiconductor is limited to the maximum concentration of $10^{19}\frac{dopants}{cm^3} = 10^{-2}\frac{dopants}{nm^3}$, over which the material is considered degenerate at room temperature.[3] This means that typically there is less than a single dopant per cubic nanometer, thus making it almost impossible to create a doping-controlled charge separation at the nanoscale.

In recent years, studies of electron transfer through organic helical chiral molecules have shown that electron transmission through these molecules is spin dependent at ambient temperatures.[4,5] Particularly, it has been revealed that chiral helical molecules can serve as efficient spin filters due to strong spin orbit coupling mechanisms and different spin transfer probabilities,[6–13] thus creating a chiral-induced spin selectivity (CISS) effect.

The spin selectivity of charges transported through chiral molecule is dependent on the charge sign, the current direction, and on the handedness of the molecule.[8] Therefore, by controlling the electron-hole spin states in nanostructures, using different circularly polarized light excitation, we affect the probability of the charges with certain spin to be transferred through the chiral monolayer. Similar behavior was observed in the study of local spin-based magnetization via charge transfer in self-assembled monolayer (SAM) of chiral polyalanine molecules.[5]

Semiconductor nanocrystals (NCs), often called quantum dots, are very versatile due to the tunability of their optical and electronic properties by their size, shape and composition,[14,15] making them ideal for photonic devices. Photoexcitation of a strongly confined NC system such as CdSe, results in the formation of excitons with known spin states.[16] Previous experiments have shown processes of a fast hole spin-flip in CdSe NCs, which enables the creation of electron-hole pairs with equal sign of spin states $(S_e, S_h)_{\pm 1/2, \pm 3/2}$.[17–19] The spin direction is then dependent on the circular polarization of the exciting light.[20,21] By using organic molecules, covalent selective adsorption of the CdSe NCs can be achieved.[22] For example, by coupling the NCs to a field effect transistor (FET), our group has previously shown that a room temperature spectrally tunable light detector can be realized.[23] In the present study we demonstrate nano scale charge separation using a thin layer device based on helical chiral molecules and semiconductor NCs. We combined a SAM of polyalanine with NCs and measured the induced photocurrent when the NCs are illuminated with light polarized in different ways. By applying circularly polarized light it was possible to generate charge separation in this system. The significant difference in the current responses on the nano metric scale was attributed to the CISS effect and to room temperature charge separation. Similar devices can be simply fabricated in large scale and can be adapted to a wide variety of NCs.

[Results]

Current response was measured under illumination with different light polarizations – clockwise (CW), counter clockwise (CCW) and linear. The I–V curves are displayed in figure 2a. The dark current (black line) has a diode-like shaped feature resulting from the $Au - NCs - ITO$ interface in the device. The illuminated measurements show a conductance that is light polarization dependent. This response is governed by both coherent spin relaxation processes and fast non coherent processes.[24] In order to retain solely the polarization dependence for the current response, we subtract the linear polarization response from the CCW and CW circular polarization (Figure 2b). In negative bias the CW circular polarization response is stronger while in forward bias the CCW polarization has a stronger response. In both cases, the holes and electrons are separated but with different efficiencies. Since linear polarization carries both CW and CCW circular polarization probabilities equally, smaller charge separation effect should be observed.

By selectively controlling the electron-hole spin states with different circularly polarized light we affect the probability of the charges transfer through the chiral monolayer. CW and CCW circular polarized light creates electrons with favored or unfavored spin states according to the CISS effect where the charge transfer probability is dependent on the charge sign as well as on the favored spin state.[25] These electrons are driven through the chiral molecules once a negative voltage bias is applied. For a given bias voltage on the device we expect higher current for a selected circular polarization than the counter circular polarization. Furthermore, this trend is expected to flip once the bias voltage is reversed, giving rise to antisymmetric I-V curves for negative and positive biases. For our chiral SAM, CW polarized light creates electrons with favored spin states, while the holes don't have the required spin state to be transferred through the chiral molecules, therefore charge separation is created. This effect is schematically portrayed in

Figure 4a where the device is under illumination of CW circular polarized light, and a negative bias is applied. The light creates electron-hole pairs with spin facing up, and the bias drives the electrons downwards through the chiral molecules. The spin and charge values of these electrons are favored by the CISS effect, therefore the current will be higher than electrons with spin down (CCW polarization) or holes with spin up (positive bias). In a general energetic perspective, a model is suggested in Figure 4b, with a pseudo CISS gap that changes according to the polarization on the device. Charges carrying the favored spin, will have energetic preference to transfer through the chiral monolayer.

The I-V difference observed under different excitation polarizations, due to the CISS effect, is diminished once higher voltages are applied, at approximately 2 volts, as shown in Figure 2b inset for negative bias. This can be explained by the strength of the spin-orbit coupling (SOC) of the charge passing through a chiral monolayer with the chiral potential.[25,26] In the literature, similar response of $0.5\ eV$ was measured for helical chiral double stranded DNA oligomers.[25] Twice this value is assigned to be the energy gap between two different spin states. Therefore we can assume that the CISS pseudo-gap for polyalanine is in the same order of magnitude, around 1eV.

Measurements of the change in current response with the tuning of the light illumination flux and polarization measured at a constant negative bias voltage of $-1.5\ Volts$ show that the CCW circular polarization had the weakest current response similarly to the previous I-V measurement, while CW circular polarization had the strongest current with the linear polarization in between these two (Figure 2c). The CISS response does not grow linearly with the intensity of the excitation. This can be ascribed to the fact that at high excitation power the Auger process, which does not conserve spin, becomes dominant. As expected, the linear response is somewhat between the CCW and CW circular polarization response. This agrees with the understanding that linear

polarization holds equal components of CCW and CW polarizations, thus creating also an equal amount of opposite spin carriers in the NCs. Therefore we should expect that the linear response would be the sum of the response of both circular polarizations at half the intensity. However, the linear response is closer to CW response, and the difference could be ascribed to the non-linearity of the collective spin coherence time T2 decay at different intensities and polarizations.[27]

We measured the absolute response of the device with chiral molecules and 610 *nm* CdSe NCs, under different illumination wavelengths and polarizations and compared them to a reference sample without NCs. The absolute response for the device is shown in figure 3a. It was calculated by subtracting the dark current response from the polarized (CW or CCW) response, then by normalizing it with the dark current response. Figure 3a presents the device behavior with above band gap illumination-532 *nm* (red curves), and below-the-band gap 660 *nm* illumination (blue curves). As a reference we measured a device without the NCs layer on top of the chiral molecules. The device with chiral molecules and NCs, illuminated above band gap has a response two orders of magnitudes larger than the device with below band gap illumination, and four orders of magnitude larger than the device without NCs. Moreover, the fact that the absolute response is dependent on the bias agrees well with the diode-like characteristics of the NCs junction, unlike the reference measurements where the absolute response is constant. From these measurements we presume that the previous I-V measurements can be mainly attributed to charges created in the NCs.

The asymmetry between the circular polarizations normalized to the linear response was calculated for four different devices (Fig. 3b). This was done by subtracting the linear current response from the circular polarization responses, then normalizing it by dividing by the linear current response. In this figure we compared the influence of the chirality of the molecules and

NCs size on the performance of the devices. For the device with chiral molecules and *610 nm* CdSe NCs (red curve) a distinct asymmetry is seen between CW and CCW illuminations, especially in the negative bias. This is peculiar since the asymmetry difference is measured in the device in spite of its narrow layer (~4 nm) of the chiral molecules. The difference is much smaller at the positive bias which agrees with Figure 2b, where the CCW polarization becomes stronger in positive biases, thus showing spin coherence influence on charge separation. To further study the effect and connect it with the spin coherence time, measurements were performed with a monolayer of smaller CdSe NCs, with the main emission peak at 520 *nm*, adsorbed on top of the chiral monolayer. The bandgap of the smaller NCs was closer to the excitation laser's wavelength of 532nm, which would enable better spin coherence since only a narrow-energy ensemble of dots is excited exactly to the bandgap.[21] On the other hand, in previous studies of smaller CdSe NCs (with the absorption peak of 498 nm and 578 nm) a fast electron spin state flip was measured.[21] Overall shorter spin coherence T1 times are expected to be shorter with smaller dots. This compromises the charge separation process in our device configuration. The asymmetry measurements for the smaller CdSe NCs, shown in green in Figure 3b, demonstrate a spin dependant charge separation effect that is weaker than for the larger NCs. Thus the measurements seem to be sensitive to the spin coherent time of the dots and to the electron spin flip, which in the case of smaller CdSe NCs becomes more dominant and compromises the charge separation effect.

Smaller charge separation effect could be also predicted due to changes in the excited states lifetime upon cooling. Spin coherence and excited states life times are expected to be two orders of magnitude larger at low tempertures.[28,29,30] However, in the helical chiral molecules it has been shown that below 150*K* the chiral molecules used in this study undergo structure phase transition thus rendering a weak spin selectivity CISS effect.[31,32] Upon cooling one would expect an increase

of charge separation down to 150K with the effect disappearing at lower temperatures. For a cooled down system (blue curves) and reference room temperature measurements of non-chiral *1,9-nonanedithiol* (9DT) molecules (black curves) the asymmetry is much lower indicating negligible CISS effect in the devices. Indeed at 55K the asymmetry results for the chiral molecules (in blue) are similar for both circular polarizations, and are all weak relatively to the room temperature measurements, indicating that the CISS effect is less prominent at low temperatures.

In conclusion, we have demonstrated nano scale charge separation using a thin layer device based on chiral molecules and semiconductor NCs. We have shown that the device was sensitive to the circular polarization excitation of the NCs, measuring a difference in the current responses in our device. The measured difference was attributed to the CISS effect and to room temperature charge separation at the small 4nm scale. Our measurements were susceptible to the spin states dynamics (electron and hole spin flip times) of the excitons created in the NCs, which are dependent on the size of the NCs used. Similar effects for small scale charge separation are measured in biological photosynthetic systems where the molecules are chiral as well. In the future, devices using the measured effect could be fabricated with nano sized features.

[Methods]

The charge separation device was fabricated using upper and lower contacts with adsorbed molecules and NCs in between, as shown in Figure 1a. 150 nm lower gold contacts were evaporated and pattered, using conventional photo-lithography methods, on SiO_2 substrate followed by a dielectric insulation layer of 150 nm Al_2O_3. The device active area was attained by wet etching $40 \times 50\ \mu m^2$ windows in the Al_2O_3 layer down to the lower contact, followed by a selective adsorption of the chiral, charge separation layer and the CdSe NCs on top of the gold bottom contact. A 4–7-nm thick Al_2O_3 tunnel barrier was evaporated in a cooled chamber on top of the NCs followed by a top transparent indium tin oxide (ITO) contact. To achieve better statistics, many windows were opened in each device (as shown in Figure 1a). The full device was mounted and wire bonded to a 44 header chip (Figure 1b). A close up of the active area is shown in the inset of Figure 1b.

The adsorbed hybrid (chiral molecule-NCs) layer was realized by chemically connecting the desired NCs to a self-assembled monolayer of molecules on top of the gold contacts. α helix L-polyalanine (AHPA-L) molecules (Sigma-Aldrich Co. LLC), diluted to a 1-mM ethanol solution were used as covalent chiral linkers. 1,9-nonanedithiol (9DT) (Sigma-Aldrich Co. LLC) non-chiral molecules were used for reference measurements. Two types of core CdSe NCs were studied, one with main emission peak at 610 nm and one at 520 nm (Sigma-Aldrich Co. LLC) with 40nm distribution widths. The NCs solution was further diluted in toluene solvent to the concentration of $0.5\frac{mg}{ml}$.

The hybrid layer preparation was performed in three steps. First, the devices were left in absolute ethanol for 20 min, then the devices were incubated in the ethanol solution of the organic molecules; 3 hours for chiral molecules or overnight for 9DT molecules. The excess of the organic

molecules was removed from the surface by washing the sample with ethanol several times. Lastly, the samples were dried under nitrogen and introduced into a toluene solution containing the NCs for 4 hours. The whole process was performed under inert atmosphere. Figure 1c displays a SEM micrograph of the adsorbed CdSe NCs on top of a chiral monolayer.

The NCs were optically excited with a diode-pumped solid-state continuous-wave (DPSS CW) 532 nm (660 nm) laser with typical laser power of 20 mW. The clockwise (CW) or counter clock wise (CCW) circular polarization illumination was achieved using a linear polarizer in the optical path (45° or 315°, accordingly) followed by a quarter wave plate. The ensuing constant laser intensity was monitored using a detector during measurements. A simple mechanical shutter was placed along the optical path to compare light and dark measurements. I-V transport measurements were performed with Keithley 2400 source meter and 6485 pico-ammeter.

Structure of the chiral monolayer on the gold was characterized by Polarization modulation-infrared reflection-adsorption spectroscopy (PM-IRRAS) and atomic force microscopy (AFM) methods.[33,34] The PM-IRRAS spectra is displayed in Figure 1d. The information about the tilt angle of the helix axis from the surface normal can be obtained from the intensity of amide I and amide II bands which appear at $1663\ cm^{-1}$ and $1549\ cm^{-1}$, respectively[24,35] (see supplementary information). The value of the tilt angle γ of the helix with respect to the surface normal was found to be $\gamma = 46°$. The thickness of the chiral monolayer was characterized by AFM (Fig 1e). An area of about $400\ nm^2$ was removed by scratching the molecules from the surface (see inset). The uncovered area shows a depth of about $\delta = 3.0\ nm$ relative to the unscratched area. Taking into account both measurements, we observe that the chiral monolayer height is about 4.3 nm.

Supplementary – PM-IRRAS measurements

The PM-IRRAS spectra is shown in Fig 2b. The information about the tilt angle of the helix axis from the surface normal can be obtained from the intensity of amide I and amide II bands which appear at $1663\ cm^{-1}$ and $1549\ cm^{-1}$, respectively[24,35].

The orientation of the peptide molecules immobilized on the gold surface was determined using the following equation:[24] $\frac{I_1}{I_2} = 1.5 \times \frac{(3cos^2\gamma-1)(3\cos^2\theta_1-1)+2}{(3cos^2\gamma-1)(3\cos^2\theta_2-1)+2}$, where I_1 and I_2 are the absorbance of amide I and amide II bands, respectively, γ is the tilt angle of the helical axis with respect to the surface normal, and $\theta_{1,2}$ are the angles between the transition moment and the helix axis. The values of θ_1 and θ_2 were set to $39°$ and $75°$, respectively [24]. The value of the tilt angle γ of the helix with respect to the surface normal was found to be $\gamma = 46°$

FIGURES

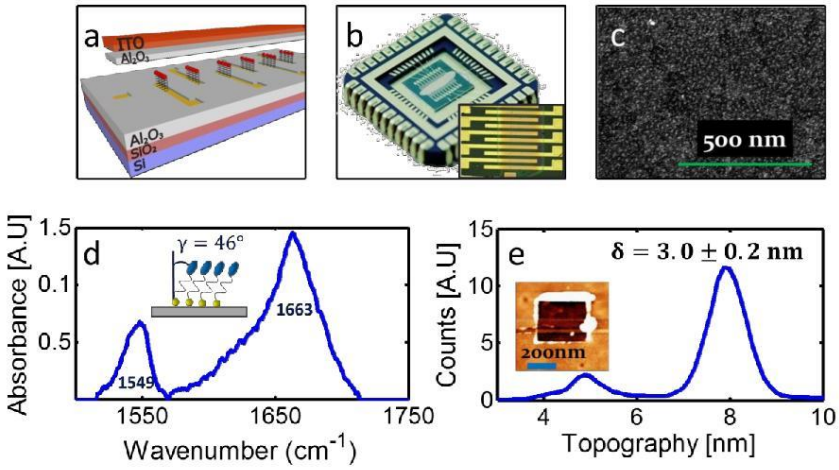

Figure 1. (a) - Schematic drawing of the device structure. I-V measurements are done between the lower gold and upper ITO contacts. (b) - Photo of device mounted and wire bonded to a 44 header chip. In the inset is a microscope picture of the active area in the device. (c) - SEM image of CdSe NCs with the main emission peak at 610 *nm*, adsorbed on top of a chiral molecules monolayer on gold. (d) - PM-IRRAS spectra of L-polyalanine monolayer on a gold surface. The energies of amide-I and amide-II vibrations indicate that the monolayer is in a helix form. From their ratio the tilt angle of the molecules adsorption relatively to the surface normal can be obtained. (e) - Histogram of the topography information of the sample surface where a portion of the chiral monolayer was removed in the middle (inset) measured by AFM. The height difference between the surface and scratched area implies that the layer thickness is 3 *nm*.

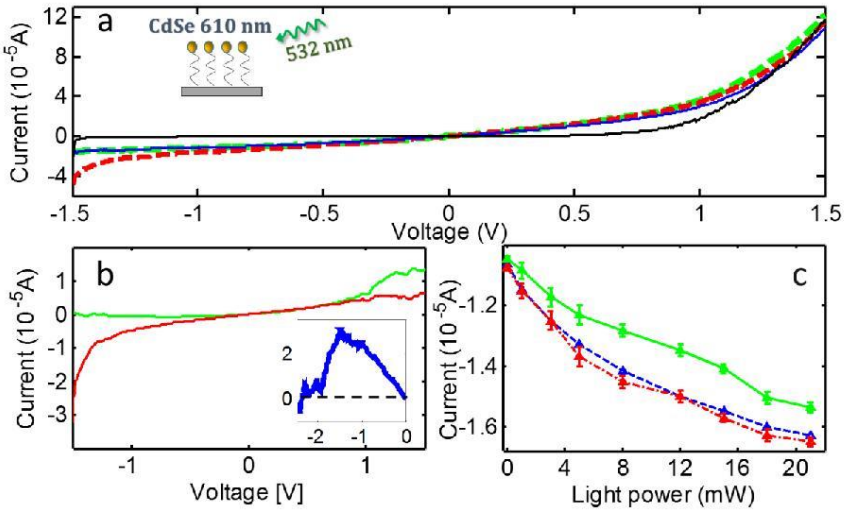

Figure 2. (a) - I-V curve of a device with adsorbed CdSe NCs (610 *nm* main emission peak) on top of helical chiral molecules, under polarized light illumination. The I–V curves for the three illumination polarizations (Red– CW, Blue – linear, Green – CCW), show distinct current responses stronger than the dark current (black). (b) - CCW (green) and CW (red) polarization current responses after the linear current was subtracted from them. The CW polarization creates electrons with favored spins, which are driven with less resistance through the chiral molecules for reversed voltage bias. On the other hand, the holes do not have the required spin state, therefore in forward bias the CCW polarization has a stronger response. In the inset the response difference between CCW and CW circular polarizations with bias extended to -2.5 V is plotted. The current difference between polarizations diminishes when the bias voltage reaches about 2 Volts, possibly due to the CISS pseudo-gap. (c) – Current response as function of excitation power for different light polarizations (Red – CW, Blue – linear, Green – CCW) under a constant bias of -1.5 Volts.

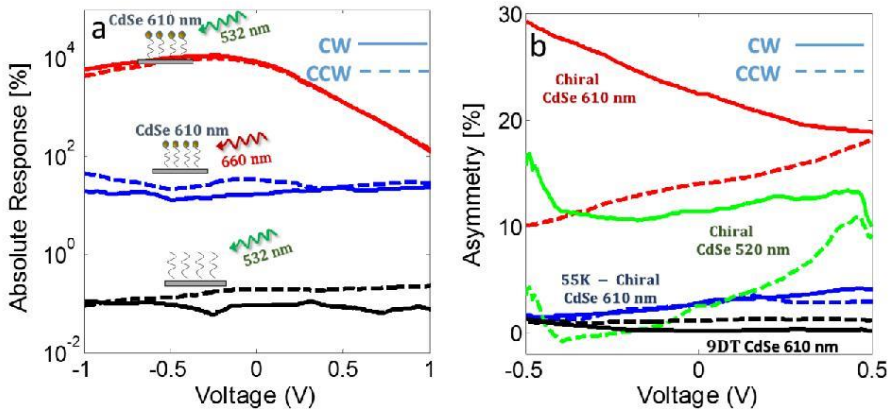

Figure 3. (a) – Absolute response of three different setups, comparing the CW (solid) and CCW (dashed) response to dark current response and giving information whether the devices react to the illuminations. As seen, the device with chiral molecules and NCs (red curves) illuminated above bandgap has a response two orders of magnitude larger than a device with below band gap illumination (blue curves) and four order of magnitude larger than a device without NCs (black curves). (b) - Asymmetry between the circular polarization normalized to the linear response, for four different devices. For the device with chiral molecules and 610 nm CdSe NCs (red curves) a distinct asymmetry is seen between CW and CCW illuminations, especially in the negative bias, thus showing long spin coherence times, enabling a more efficient charge separation. This asymmetry is slightly smaller for smaller NCs (green curves) which are known to have a shorter electron spin flip time, affecting the coherence of the states. For a cooled down system at 55K (blue curves) and reference of non-chiral 9DT molecules (black curves) the asymmetry is much lower indicating no CISS effect in the devices.

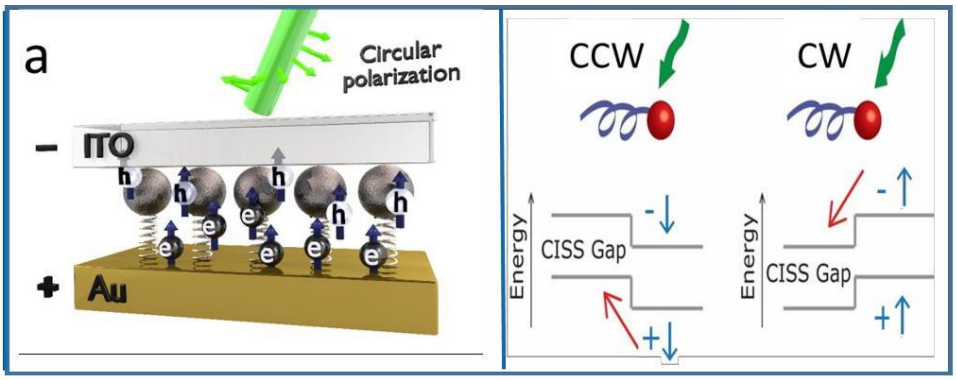

Figure 4. (a) - Schematic representation of the charge separation process in the device. Electron-hole pairs are created when exciting with a laser, CW in this example, with spins facing up. As long as the spin state is preserved under negative bias the CISS effect prefers the transfer of the electrons through the chiral monolayer. (b) In a more general energetic perspective, there is a pseudo CISS gap which changes according to the exciton polarization on the NCs. Charges carrying the favored spin, will have energetic preference to transfer through the chiral monolayer.

16

AUTHOR INFORMATION

Corresponding Author

***Y.Paltiel, Department of Applied Physics, The Hebrew University of Jerusalem, Givat Ram, Jerusalem 91904, Israel. paltiel@mail.huji.ac.il**

Author Contributions

Experimental measurements and analyzing the data was done by N. Peer. Dr. S. Yochelis helped with the chemical aspects of the work. Dr. I. Dujovne helped with the optical measurements. Y. Paltiel supervised the work. The manuscript was written with contributions from all the authors. All authors have approved the final version of the manuscript.

FUNDINGS

Funding of this project was done by the Volkswagen Foundation, the ministry of science MOS Israel, and by Yissum, the I.P. Company of the Hebrew University of Jerusalem.

ACKNOWLEDGMENTS

We acknowledge the financial support by the Volkswagen Foundation, the Ministry of Science Technology and Space, 210514 and Yissum, the I.P. Company of the Hebrew University of Jerusalem.

ABBREVIATIONS

CISS, chiral-induced spin selectivity; SAM, self-assembled monolayer; NC, nanocrystals; FET, field effect transistor; CW, clockwise; CCW, counter clockwise; SOC, spin-orbit coupling; 9DT, 1,9-nonanedithiol; ITO, indium tin oxide; AHPA-L, α helix L-polyalanine; DPSS CW, diode-pumped solid-state continuous-wave; PM-IRRAS, Polarization modulation-infrared reflection-adsorption spectroscopy; AFM, atomic force microscopy;

REFERENCES

(1) Reed, G. . *Silicon* Photonics; Reed, G. T., Ed.; John Wiley & Sons, Ltd: Chichester, UK, 2008.

(2) Shah, a. V.; Platz, R.; Keppner, H. Thin-Film Silicon Solar Cells: A Review and Selected Trends. *Sol. Energy Mater. Sol. Cells* **1995**, *38*, 501–520.

(3) Carlson, R. O. Electrical Properties of Near-Degenerate Boron-Doped Silicon. *Phys. Rev.* **1955**, *100*, 1075–1078.

(4) Nitzan, A.; Ratner, M. a. Electron Transport in Molecular Wire Junctions. *Science* **2003**, *300*, 1384–1389.

(5) Ben Dor, O.; Yochelis, S.; Mathew, S. P.; Naaman, R.; Paltiel, Y. A Chiral-Based Magnetic Memory Device without a Permanent Magnet. *Nat. Commun.* **2013**, *4*, 2256.

(6) Göhler, B.; Hamelbeck, V.; Markus, T. Z.; Kettner, M.; Hanne, G. F.; Vager, Z.; Naaman, R.; Zacharias, H. Spin Selectivity in Electron Transmission through Self-Assembled Monolayers of Double-Stranded DNA. *Science* **2011**, *331*, 894–897.

(7) Xie, Z.; Xie, Z.; Markus, T. Z.; Cohen, S. R.; Vager, Z.; Gutierrez, R.; Naaman, R. Spin Specific Electron Conduction through DNA Oligomers. *Nano Lett.* **2011**, *11*, 4652–4655.

(8) Naaman, R.; Waldeck, D. H. Chiral-Induced Spin Selectivity Effect. *J. Phys. Chem. Lett.* **2012**.

(9) Yeganeh, S.; Ratner, M. a.; Medina, E.; Mujica, V. Chiral Electron Transport: Scattering through Helical Potentials. *J. Chem. Phys.* **2009**, *131*.

(10) Medina, E.; Floralba, L.; Ratner, M. A.; Mujica, V. Chiral Molecular Films as Electron Polarizers and Polarization Modulators. 1–5.

(11) Gutierrez, R.; Díaz, E.; Naaman, R.; Cuniberti, G. Spin-Selective Transport through Helical Molecular Systems. *Phys. Rev. B* **2012**, *85*, 081404.

(12) Gersten, J.; Kaasbjerg, K.; Nitzan, A. Induced Spin Filtering in Electron Transmission through Chiral Molecular Layers Adsorbed on Metals with Strong Spin-Orbit Coupling. *J. Chem. Phys.* **2013**, *139*.

(13) Skourtis, S. S.; Beratan, D. N.; Naaman, R.; Nitzan, A.; Waldeck, D. H. Chiral Control of Electron Transmission through Molecules. *Phys. Rev. Lett.* **2008**, *101*, 238103.

(14) Peng, X.; Manna, L.; Yang, W.; Wickham, J.; Scher, E.; Kadavanich, A.; Alivisatos, A. Shape Control of CdSe Nanocrystals. *Nature* **2000**, *404*, 59–61.

(15) Mocatta, D.; Cohen, G.; Schattner, J.; Millo, O.; Rabani, E.; Banin, U. Heavily Doped Semiconductor Nanocrystal Quantum Dots. *Science* **2011**, *332*, 77–81.

(16) Klimov, V. *Nanocrystal Quantum Dots*; 2010.

(17) Kim, J.; Wong, C. Y.; Scholes, G. D. Exciton Fine Structure and Spin Relaxation in Semiconductor Colloidal Quantum Dots. *Acc. Chem. Res.* **2009**, *42*, 1037–1046.

(18) Huxter, V. M.; Kim, J.; Lo, S. S.; Lee, A.; Nair, P. S.; Scholes, G. D. Spin Relaxation in Zinc Blende and Wurtzite CdSe Quantum Dots. *Chem. Phys. Lett.* **2010**, *491*, 187–192.

(19) Horodyska, P.; Nemec, P.; Sprinzl, D.; Maly, P.; Gladilin, V. N.; Devreese, J. T. Exciton Spin Dynamics in Spherical CdS Quantum Dots. **2010**, 24.

(20) Němec, P.; Nahálková, P.; Sprinzl, D.; Malý, P.; Gladilin, V. N.; Devreese, J. T. Spin-Sensitive Differential Transmission Experiments in Quasi-Spherical CdS Quantum Dots. *Phys. status solidi* **2006**, *3*, 4291–4294.

(21) Ma, H.; Jin, Z.; Zhang, Z.; Li, G.; Ma, G. Exciton Spin Relaxation in Colloidal Cdse Quantum Dots at Room Temperature. *J. Phys. Chem. A* **2012**, *116*, 2018–2023.

(22) Koslovsky, O.; Yochelis, S.; Livneh, N.; Harats, M. G.; Rapaport, R.; Paltiel, Y. Simple Method for Surface Selective Adsorption of Semiconductor Nanocrystals with Nanometric Resolution. *J. Nanomater.* **2012**, *2012*, 1–5.

(23) Neubauer, A.; Yochelis, S.; Amit, Y.; Banin, U.; Paltiel, Y. Highly Sensitive Room Temperature Infrared Hybrid Organic-Nanocrystal Detector. *Sensors Actuators A Phys.* **2015**, *229*, 166–171.

(24) Miura, Y.; Kimura, S.; Imanishi, Y.; Umemura, J. Formation of Oriented Helical Peptide Layers on a Gold Surface Due to the Self-Assembling Properties of Peptides. *Langmuir* **1998**, *14*, 6935–6940.

(25) Naaman, R.; Waldeck, D. H. Chiral-Induced Spin Selectivity Effect. *J. Phys. Chem. Lett.* **2012**, *3*, 2178–2187.

(26) Winkler, R. *Spin-Orbit Coupling Effects in Two-Dimensional Electron and Hole Systems, Issue 191*; Springer Science & Business Media, 2003.

(27) Uskov, a. V.; Boucher, Y.; Le Bihan, J.; McInerney, J. Theory of a Self-Assembled Quantum-Dot Semiconductor Laser with Auger Carrier Capture: Quantum Efficiency and Nonlinear Gain. *Appl. Phys. Lett.* **1998**, *73*, 1499–1501.

(28) Donegá, C. D. M.; Bode, M.; Meijerink, A. Size- and Temperature-Dependence of Exciton Lifetimes in CdSe Quantum Dots. **2006**, 1–9.

(29) Syperek, M.; Yakovlev, D.; Yugova, I.; Misiewicz, J.; Sedova, I.; Sorokin, S.; Toropov, a.; Ivanov, S.; Bayer, M. Long-Lived Electron Spin Coherence in CdSe/Zn(S,Se) Self-Assembled Quantum Dots. *Phys. Rev. B* **2011**, *84*, 1–8.

(30) Zhang, Z.; Jin, Z.; Ma, H.; Xu, Y.; Lin, X.; Ma, G.; Sun, X. Room-Temperature Spin Coherence in Zinc Blende CdSe Quantum Dots Studied by Time-Resolved Faraday Ellipticity. *Phys. E Low-Dimensional Syst. Nanostructures* **2014**, *56*, 85–89.

(31) Dor, O. Ben; Morali, N.; Yochelis, S.; Baczewski, L. T.; Paltiel, Y. Local Light-Induced Magnetization Using Nanodots and Chiral Molecules. *Nano Lett.* **2014**, *14*, 6042–6049.

(32) Carmeli, I.; Kumar, K. S.; Heifler, O.; Carmeli, C.; Naaman, R. Spin Selectivity in Electron Transfer in Photosystem I. *Angew. Chemie* **2014**, *126*, 9099–9104.

(33) López-Pérez, D. E.; Revilla-López, G.; Jacquemin, D.; Zanuy, D.; Palys, B.; Sek, S.; Alemán, C. Intermolecular Interactions in Electron Transfer through Stretched Helical Peptides. *Phys. Chem. Chem. Phys.* **2012**, *14*, 10332–10344.

(34) Naaman, R.; Vager, Z. Spin Selective Electron Transmission through Monolayers of Chiral Molecules. *Top. Curr. Chem.* **2011**, *298*, 237–257.

(35) Kennedy, D. F.; Crisma, M.; Toniolo, C.; Chapman, D. Studies of Peptides Forming 310- and .alpha.-Helixes and .beta.-Bend Ribbon Structures in Organic Solution and in Model Biomembranes by Fourier Transform Infrared Spectroscopy. *Biochemistry* **1991**, *30*, 6541–6548.

Appendix C – Published paper: Nano bio optically tunable composite nanocrystalline cellulose films:

RSC Advances

PAPER

View Article Online
View Journal | View Issue

Cite this: *RSC Adv.*, 2015, **5**, 7713

Nano bio optically tunable composite nanocrystalline cellulose films

Y. Nevo,†[a] N. Peer,†[b] S. Yochelis,[b] M. Igbaria,[c] S. Meirovitch,[c] O. Shoseyov*[a] and Y. Paltiel*[b]

Plastic pollution creates major environmental damage especially when taking into account the constant increase in the use of plastic films. Therefore, increasing the use of biodegradable films and reducing non degradable plastic usage are worldwide necessities. Current biodegradable films are not transparent or strong enough for most applications. In this work we utilize nanocellulose and semiconductor nanocrystals to reinforce and functionalize a biodegradable transparent film to create a transparent, strong and optically tunable plastic film. Nanocrystalline cellulose is produced from cellulose fibers, the main component of plant cell walls. The nanocrystalline cellulose particles are 5–20 nm in diameter, a few hundreds of nanometers in length, and have superb mechanical properties. The optical properties are controlled by introducing nanocrystals within the nanocellulose layers. The hybrid nanocellulose/nanocrystals film reinforcement will enable the reduction in the amount of plastic polymer in most polymeric materials while maintaining mechanical integrity with additional optical properties.

Received 6th October 2014
Accepted 16th December 2014

DOI: 10.1039/c4ra11840e

www.rsc.org/advances

Introduction

The routine and extensive use of plastic films composed of such materials as polyethylene (PE), polyethylene terephthalate (PET) and polypropylene (PP) has greatly increased, becoming a major environmental concern. The ability to reduce the amounts of such polymers in polymeric articles while maintaining mechanical integrity and endowing the materials with optical properties, has thus far been proved unsuccessful. In this work we utilize nanocrystalline cellulose (NCC) and semiconductor nanocrystals (NCs) with unique characteristics to produce transparent strong films with tunable optical properties. These reinforced films can reduce the thickness of required non-degradable PE, PET or PP, or they can enhance the properties of degradable films, such as poly(lactic acid) (PLA).

NCC, produced by hydrolysis of cellulose fibers has attracted a lot of attention due to its physical, chemical and mechanical properties. A variety of cellulose sources can be used in order to produce NCC, such as cotton,[1] wood,[2] bacterial cellulose,[3,4] microcrystalline cellulose (MCC),[5] and even recycled wood pulp, which is present in waste streams of paper mills and municipal sewage system sludge. The use of sulfuric acid in the hydrolysis process results in rod-shaped nanoparticles, which are negatively charged due to the formation of sulphate ester groups on their surface, leading to a well dispersed and stable water suspension. Above a certain critical concentration, the NCC suspension can form ordered liquid crystal phases.[6] The advantages of NCC, namely its superb properties, renewability, biodegradability and abundance, lead to its recognition as one of the most promising materials for future applications. NCC is nearly as strong as Kevlar and can be added to materials to increase their strength and stiffness.[7–10] Many studies in recent years have shown that NCC can be used as a building block in a variety of applications. The most common use of NCC is as filler in nanocomposite materials[11–13] but it has also been utilized in other applications such as adhesives,[14,15] foams, aerogels[16,17] and films.[18–20]

Upon drying, NCC liquid crystal water suspension is known to self-assemble into macro scale ordered films, as seen in Fig. 1a.

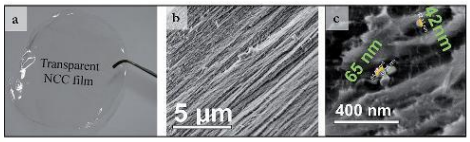

Fig. 1 (a) Dried NCC film. (b) SEM micrograph of an independent NCC film prepared with ZnO NCs. (c) Zoomed in SEM micrograph of an independent NCC film prepared with ZnO NCs. Note the ZnO NCs located between the layered films.

[a]The Robert H. Smith Institute of Plant Sciences and Genetics in Agriculture, The Hebrew University of Jerusalem, Rehovot 7610001, Israel. E-mail: paltiel@mail.huji.ac.il

[b]Department of Applied Physics, The Hebrew University of Jerusalem, Givat Ram, Jerusalem 9190401, Israel. E-mail: shoseyov@agri.huji.ac.il

[c]Valentis Nanotech Ltd, Industrial Zone, Misgav 2017900, Israel

† The first two authors contributed equally to the work. They were helped by Dr S. Yochelis from Paltiel Lab and Mr M. Igbaria and Dr S. Meirovich from Valentis Nanotech. O. Shosayov and Y. Paltiel supervised the work. All authors wrote the paper jointly.

NCC films can be transparent or semitranslucent and can retain the liquid crystalline order of the suspension.[21] Furthermore, NCC-based films and composite material were found to have good gas barrier properties, attributed mainly to the high crystallinity of the nano crystals which lower the diffusion of gas molecules and elongate the path they travel through the film.[22] Alone or combined with other materials, self-assembled NCC films with intriguing properties enable cost effective, tunable coatings for large surfaces.

Quantum dots are quantum confined structures in all three dimensions.[23] Consequently, electrons and holes occupy discrete energy states. Furthermore electrons in quantum dots buried in a quantum well may tunnel from one dot to the next. This gives rise to delocalization effects and to the creation of minibands which are of considerable scientific interest.[24] These unique quantum properties have attracted in recent years a great deal of scientific and technological interest. From the applications point of view quantum dots allow the use of quantum mechanics in the real world of ambient temperature operating devices. Such devices include optoelectronic,[25,26] quantum information processing[27,28] and energy harvesting devices.[29,30] In particular semiconductor quantum dots have a large potential for applications in optoelectronics.[31]

Semiconductors quantum dots, referred in this article as semiconductor nanocrystals (NCs), are emerging as useful building blocks of electro-optical devices, due to their size, composition and shape dependent photoluminescence.[32,33] using the same NCS and changing their size will create optical tunability of the absorption. For example, InAs-based NCs are tunable in the near-infrared (NIR), effectively covering the telecom range. In recent years simple cheap methods were developed to fabricate highly efficient quantum dots.[34,35] An appealing feature of such colloidal systems is the chemical accessibility allowing flexible processing. InAs and PbS NCs light-emitting diodes operating in the NIR were embedded within a semiconductor polymer matrix.[36–38] InAs colloidal dots were also incorporated in waveguide structures[33] and evidence for optical gain has recently been reported.[32] The chemical accessibility of the colloidal NCs also enables to link them to different surfaces.[39] Moreover, efficient emission has been reported for CdSe dots deposited on surfaces of quantum wells, introducing an additional attractive method for electrical activation of their fluorescence.[40] Recently, it has been demonstrated that the electronic properties of semiconductor-based devices can be modified by organic molecules adsorbed on their surfaces.[41] Therefore, the combination of organic molecules and NCs can further enhance the ability to control properties of the hybrid system.

In the presented work we have combined the NCC properties with the NCs to fabricate strong, optically controlled, biodegradable films that have the potential for many applications such as green houses and food packaging. We have used thin self-assembled layers of NCC to trap NCs inside the NCC films. The NCs can be well dispersed within NCC films, as seen in Fig. 1c. For both greenhouses and packaging applications the optical tunability of the absorption spectrum as well as mechanical reinforcement and gas barrier properties are needed. For food packaging it is critical to block UV light transmission in order to prevent the peptides denaturation[42] and photo oxidation of essential oils.[43] In greenhouses UV can reduce insect parasites navigation capabilities[44] and infrared absorption enhances the efficiency of the greenhouse.[45,46]

Methods

The fabrication process includes three stages: (a) the NCC was produced by acid hydrolysis of the amorphous weak parts of cellulose fibers. After the hydrolysis we wash the acid and finally, we use sonication in order to get a homogeneous, clear solution of NCC. (b) The NCs solution was mixed with the NCC solution in different ratios and finally (c), it was dried upon a plastic Petri dish or plastic film – PE, biaxially oriented polypropylene (BOPP) and PET.

NCC production was based on the method of Pranger and Tannenbaum.[47] Micro Crystalline Cellulose (MCC, Avicel®, FMC Biopolymer Inc.) was hydrolized in 63 wt% H_2SO_4 at a temperature of 60 °C with stirring, for 2 hours. Following the hydrolysis, the suspension was centrifuged at 10 000 rpm for 10 min. Acid was removed and the pellet was resuspended in deionized water (DIW). The washing and resuspension cycles were repeated for 4 to 5 times until the supernatant coming out of the centrifuge was turbid and the pH of the supernatant was approximately 2. Following the final wash the suspension was dialyzed against DIW for 2 weeks. After dialysis, the suspension was neutralized using NaOH followed by sonication treatment [CL4 ultrasonic convertor, Misonix] that lead to a clear NCC suspension.

At the second stage, we prepared the NCs solutions. We used ZnO Ag doped NCs (M K Impex Corp, ZnO (70 nm) doped with silver, 50 wt% in H_2O, colloidal dispersion) in order to absorb the UV light. ZnO has a wide band gap of 3.37 eV which means it absorbs light with wavelengths lower than 370 nm.[48] Ag doping of ZnO allows a tunable redshift of the NCs due to the shrinkage of the band gap energy.[49,50] Furthermore, ZnO NCs were found to be biocompatible and biodegradable.[51] The ZnO Ag doped NCs solution was further diluted in H_2O in the ratio of 1 : 500. We also used SiO_2 NCs (Meliorum Technologies SiO_2–H_2O, 5 nm PPS, 50 mg/30 mL) in order to block the long wave infrared spectra emitted at room temperature from the greenhouse ground. In this way we could mimic the optical properties of glass and enable better energy conservation of the greenhouse, while maintaining the film flexibility. SiO_2 NCs are also known to be biocompatible and biodegradable.[52,53] The SiO_2 NCs solution was further diluted in H_2O in the ratio of 1 : 100. In order to absorb UV light and emit it in the visible spectra, we used photoluminescent CdSe/ZnS core–shell quantum dots (QD)s (MKnano, CdSe/ZnS-WS-yellow stabilized by mercaptoundecanoic acid in H_2O, emission peak 570–585 nm, 25 mg/5 mL). The NCs solution was further diluted in H_2O in the ratio of 1 : 5.

Finally, in the third stage, solutions of mixed NCC and NCs were prepared by mixing the NCs and NCC in varying ratios. The mixed solutions were then used either to achieve NCC based films only, or for coating of thin non-degradable plastic films. In order to produce NCC based films, NCC/NCs solution was dried

on a plastic Petri dish (see Fig. 1a). The diameter of the drops was 1–2 cm and their thickness was to be 50 μm. In order to coat plastic films (PE, BOPP and PET) with NCC suspension, plastic films were first pretreated using N_2-plasma [PICO UHP plasma system, Diener electronics] which makes the surface of the film positively charged. Coating of plastic films was conducted using a roll coater [K control coater, Printcoat instruments]. NCC suspensions (2 wt%), with or without NCs, were coated upon the surface of the plastic films at a desired wet thickness of 100 μm and was then left to dry. The resulted dry coating layers were ~1 μm thick. The thickness of the plastic films was 70 μm, 18 μm and 13 μm for PE, BOPP and PET, respectively. The adhesion of the coating layers to the films was tested using the adhesion tape testing method, in which a pressure sensitive tape was used to determine the adhesion quality of the coatings. This test is commonly used in industry.

The prepared samples were then optically measured in the visible spectra by illuminating them with a deuterium/halogen light source (Avantes Avalight-DH-S-BAL) and measuring the transmission with a visible-NIR spectrometer (Ocean Optics USB4000). FTIR measurements were also performed to determine the transmission and absorption in the infrared spectra (Bruker VERTEX-80V). These measurements were performed in vacuum conditions in order to eliminate atmospheric moisture absorptions. The mechanical properties of the films were investigated in both the linear and non-linear range, using an Instron machine (Instron 3345 Tester, Instron, Norwood, MA) equipped with a 100 N load cell. Samples were cut according to ASTM method D882-02 and the thickness was measured using a Mitutoyo Digimatic Indicator (Type ID-S112MB; Mitutoyo Manufacturing Co. Ltd., Tokyo, Japan) at five random positions along the film.

For the measurements of NCC as an oxygen barrier we used the dye molecule methylene blue. When oxidized the methylene blue color is transformed from orange to blue. We started with reduced methylene blue, using 0.8 g NaOH with 15 mL H_2O and 0.5 g of glucose as the reducing agent. After stirring the mixture until the solids were dissolved we added the methylene blue (0.05 g of methylene blue in 50 cm^3 ethanol). The resulting blue solution was reduced after one minute turning to orange. Under nitrogen environment we then gradually mixed agar into the solution until it became a gel. For the experiment we prepared several vials with pierced caps and under the nitrogen environment filled them with the reduced gel. We then covered some of the vials with NCC coated PET films, some with PET and some without a blocking layer as a reference. The vials were then capped with the pierced caps and taken out to room conditions.

Further measurements of the oxygen transmission rate (OTR) of the films were performed on NCC coated BOPP films, using the OX-TRAN® Model 2/21 instrument accordance with ASTM D 3985 under 23 °C and 0% RH.

Results

To demonstrate the change in mechanical properties of the new NCC and NCC/NCs coated films, tensile tests experiments were carried out. In these experiments we measured the elastic modulus, tensile stress at break, and tensile strain at break of PE, BOPP and PET films, without any treatment, after plasma pretreatment and after NCC coating (with and without NCs). As can be seen in Table 1, the elastic modulus of PE films coated with NCC increased by more than 100% in comparison to uncoated PE films.

Furthermore, we found that the addition of NCs to the NCC coat did not compromise the mechanical properties improvement. Both the stress at break and tensile strain at break did not change significantly compared to the uncoated films.

A significant increase of about 20% in the elastic modulus was also observed for coated BOPP films. Due to the very high elastic modulus of BOPP films, the increase was not as dramatic as with PE films.

The elastic modulus of stiff PET films was also improved by the NCC coating, by about 14%. Similar to the coated PE films, the tensile stress at break and tensile strain at break of coated BOPP and PET films did not change significantly.

To test the adhesion of the coatings to the film's surface, we used the adhesion tape testing method. In this experiment no adhesion failure was detected. The BOPP samples with painted NCC coating proved to strongly adhere to the film, without leaving remains of the NCC coating on the tape after being pulled.

Table 1 Mechanical properties of coated and uncoated plastic sheets. ($n = 10$, mean ± SD)

Film	Elastic modulus (MPa)	Stress at break (MPa)	Strain at break (%)
PE	194 ± 10	23 ± 1	1031 ± 41
PE plasma	228 ± 7	23 ± 1	953 ± 32
PE/NCC	414 ± 55	22 ± 1	961 ± 28
PE/NCC/ZnO (1 : 160)	351 ± 26	22 ± 1	941 ± 16
BOPP	1898 ± 100	104 ± 17	152 ± 10
BOPP plasma	1645 ± 115	100 ± 10	148 ± 10
BOPP/NCC	2377 ± 274	103 ± 10	144 ± 10
PET	4173 ± 190	150 ± 6	94 ± 9
PET plasma	4082 ± 121	150 ± 23	102 ± 7
PET/NCC	4757 ± 221	141 ± 11	92 ± 11

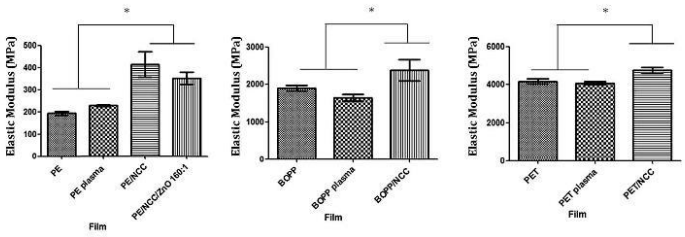

Fig. 2 Elastic modulus of the different plastic films. Elastic modulus comparison of coated and uncoated plastic films (* represents statistically significant difference, as analyzed using one way ANOVA for multiple comparison and 2-sample t-test, $p < 0.05$).

Fig. 2 summarizes the statistically significant elastic modulus enhancement of PE, BOPP and PET coated films. In the case of PE films, adding a 1 μm NCC coating to the 70 μm thick PE film was enough to greatly enhance the elastic modulus of the film. For BOPP and PET films, dry NCC layers of 1 μm thickness, coated films of 18 μm and 13 μm, respectively.

A 25 μm thick, biodegradable poly(lactic acid) (PLA) film was also coated with NCC, resulting in an increase of 65% in elastic modulus compared to uncoated film (data not shown).

As mentioned above NCs possess interesting size-dependent structural, and optical properties.[54] The ability to control the colloidal NCs growth allows one to control the structure, composition, size, and shell structure.[55] Therefore, the actual absorption spectrum of the material can be tuned using quantum effects. We used this ability to demonstrate the control over optical transmission spectra of the NCC/NCs films, while maintaining mechanical strength of the films.

This is possible as NCs are ordered between the NCC layers as seen in Fig. 1c. For application use we mainly aimed to demonstrate strong biodegradable films that transmit in the visible while blocking UV and/or mid to far wave infrared spectra (MWIR to LWIR).

Blocking UV spectrum enables better protection of crops from insects[44] and also prevents harmful UV exposure for stored food products. Blocking the far IR spectra allows a greenhouse to be more energy efficient by conserving thermal energy within the greenhouse. Around room temperature (300 K) most of the block body radiation is concentrated in 4–12 μm range. In this range the glass (SiO_2) absorption efficiency is high while standard polyethylene (PE) is mostly transparent (see Fig. 5a). Having a flexible film with glass like absorption properties is an important goal to achieve, thus improving the greenhouse efficiency in a fundamental way.

Fig. 3 shows a control of the absorption of the UV. The films prepared with ZnO·Ag NCs (at the optimal particle ratio of 1 : 160 ZnO : NCC) displayed a good absorption of light in the UV range (<400 nm) while being almost transparent in the visible range. The ZnO has the band gap of 3.3 eV,[56] that creates an absorption peak at 375 nm. Doping the ZnO with silver has shown a band-gap reduction compared to un-doped ZnO, thus creating a red-shift in its absorption.[57] The NCC with CdSe/ZnS core–shell NCs (at the optimal particle ratio of 1 : 50 CdSe : NCC) shows also good absorption in the UV range with less than 50% transmission at wavelengths lower than 400 nm, without affecting the transparency in visible light (see Fig. 3).

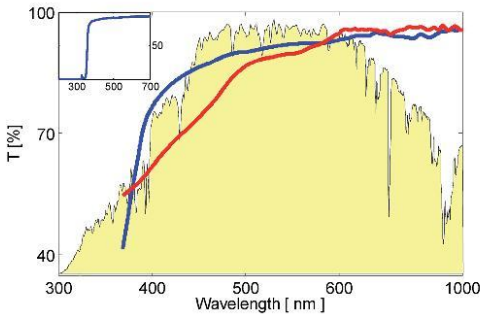

Fig. 3 UV blocking films. Transition plot in the UV and visible spectrum of NCC prepared with ZnO·Ag NCs (blue) at the particle ration of 1 : 160 ZnO : NCC, NCC prepared with CdSe/ZnS QDs at the particle ratio of 1 : 50 CdSe : NCC (red). The scaled AM 1.5 solar spectrum is also plotted (yellow). The inset shows the transmission plot of NCC/ZnO coated BOPP film.

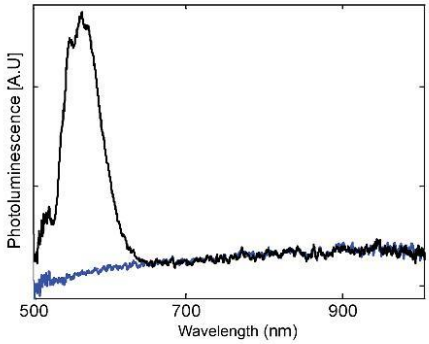

Fig. 4 UV to visible conversion films; photoluminescence plot of NCC prepared with CdSe/ZnS QDs at the particle ratio of 1 : 50 CdSe : NCC, illuminated with a 405 nm laser (black) compared to the background halogen light (blue).

This is due to the band gap of the QDs which is 2.14 eV as measured by the photoluminescence. Furthermore, in Fig. 4 the photoluminescence of CdSe/ZnO QDs is observed, while illuminating the film with a 405 nm laser, with an emission peak in the visible range at 570 nm. This demonstrates the ability to convert absorbed UV light to the visible spectra, thus enhancing the greenhouse's efficiency.

Fig. 5a is showing the visible and IR transmission spectrum of a glass, PE and NCC before modification. It is apparent that the PE, as other plastic films, is almost transparent in the visible and IR spectrum. However, while being transparent at the visible the glass has a complete cutoff around 5 μm so that the entire MWIR and LWIR spectrum is absorbed. The NCC also shows better absorption than PE in the IR spectrum. The far infrared transmission spectrum of PE films and NCC films mixed with SiO_2 is shown in Fig. 5b. The NCC and NCC/SiO_2 (at the optimal particle ratio of 1 : 150 000) films were 50 μm in thickness while the PE films were 85 μm. It can be seen that NCC shows good IR absorption. This is attributed to the typical cellulosic compounds that are assigned to C–O and C–C ring structures with absorption bands at 8.6 and 9.5 μm.[58] Another absorption band at 11 μm rises from C–O–C stretching (at the β-(1 → 4) glycosidic linkages).[59] Other external deformational vibrations of C–H, C–OH, C–CO and C–CH also add to these absorption bands.[58] The NCC with SiO_2 has the most effective absorbance in the IR range relevant for room temperature thermal emission. Thus we achieve the glass like absorption properties in flexible films. This may be due to the absorption bands of SiO_2 (typically asymmetric stretching vibration Si–O–Si bridges (9.0–9.5 μm), and the symmetric vibration stretching of the Si–O–Si bridge (~12.5 μm)).[60]

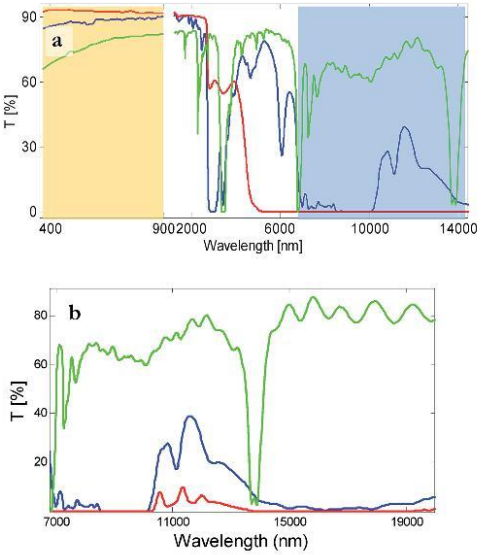

Fig. 5 Glass like NCC films; (a) visible and IR transmission spectrum of glass (red), PE (green) and NCC (blue) before any modifications. (b) IR light transmission spectrum of polyethylene greenhouse films (green) compared to NCC (blue) and NCC prepared with SiO_2 NCs at the particle ratio of 1 : 150 000 SiO_2 : NCC.

Fig. 6 Oxidation experiment with the color dye of methylene blue after 24 hours under room conditions with pierced caps. The methylene blue gel remained un-oxidized when covered with PET + NCC. When covered with PET or not covered the methylene blue oxidized.

Lastly the same films also acts as oxygen barrier as seen in Fig. 6. This is extremely important for food packaging where preventing gas flow through the package is crucial. In many standard food packages additional aluminum foils are added to prevent the oxidation and gas flow. This layer may be removed by using our films. We used the reduced dye molecule methylene blue that acts as an indicator for oxidation. The dye was placed in vials with pierced caps that were covered with the NCC + PET films. We demonstrate that the reduced methylene blue in the vial covered with the NCC + PET (polyethylene terephthalate) layer does not change its color compared to the reference vials with PET only or uncovered dye. In Fig. 6 we see the vials after 24 hours in room conditions. The dye in the NCC + PET capped vials remained orange while the other references changed their color to blue, meaning the reduced dye was oxidized while the NCC + PET was enough to protect from it oxidation.

Further measurements of the oxygen permeability of the films were performed on NCC coated BOPP films, in which the oxygen transmission rates were measured for 24 hours. The permeability of standard 20 μm BOPP films without coating is 2000 cc per m^2 per day. The results of coated BOPP films achieved a rate of less than 1 cc per m^2 per day, showing a significant improvement of the film's oxygen transmission rate. For NCC coated BOPP films the measured rate was 0.64 cc per m^2 per day. Results for NCC/ZnO coated BOPP films were 0.22 cc per m^2 per day, thus showing that the NCs do not compromise the oxygen barrier qualities of NCC but even improve them. The efficient oxygen barrier qualities are within industrial standard for most food packaging applications.

Conclusions

In this work we utilized nanocrystalline cellulose unique properties to produce a biodegradable transparent film with additional controlled optical properties. The film's optical properties were controlled by introducing nanocrystals

dispersed within the NCC layers. Following coating of plastic films with NCC, the mechanical properties of plastic films significantly improved, without being compromised by the nanocrystals addition. We showed that we increase the films modulus without reducing the stress or strain. By choosing the optimal plastic film we can achieve flexible sheet properties. These will be used to optimise the impact strength and puncture resistance for packages. We estimate that for all plastic films polymer reduction can be achieved. PE is the weakest film and therefore the largest reduction of around 30% of film thickness is expected. For BOPP and PET films reduction of 10–20% of the plastic polymer used is expected.

In future applications, NCC/NCs hybrid coatings can be used to strengthen polymers, thereby reducing the costs of materials and transport and minimizing their environmental impact, adding tunable optical and other desirable properties.

Abbreviations

PE	Polyethylene
PC	Polycarbonate
BOPP	Biaxially oriented polypropylene
NCC	Nanocrystalline cellulose
UV	Ultraviolet
IR	Infra-red
NC	Nanocrystal
NIR	Near-infrared
PLA	Polylactide acid
PET	Polyethylene terephthalate
MWIR	Mid-wave infrared
LWIR	Long-wave infrared
QD	Quantum dot

Acknowledgements

O. Shoseyov and Y. Paltiel want to acknowledge the Israel National Nanotechnology Initiative (INNI), Focal Technology Areas program and the HUJI center for nano science and nano technology.

Notes and references

1 L. Heux, G. Chauve and C. Bonini, *Langmuir*, 2000, **07493**, 8210–8212.
2 S. Beck-Candanedo, M. Roman and D. G. Gray, *Biomacromolecules*, 2005, **6**, 1048–1054.
3 M. Roman and W. T. Winter, *Biomacromolecules*, 2004, **5**, 1671–1677.
4 J. Araki and S. Kuga, *Langmuir*, 2001, 4493–4496.
5 D. Bondeson, A. Mathew and K. Oksman, *Cellulose*, 2006, **13**, 171–180.
6 J. F. Revol, H. Bradford, J. Giasson, R. H. Marchessault and D. G. Gray, *Int. J. Biol. Macromol.*, 1992, **14**, 170–172.
7 Y. Habibi, L. A. Lucia and O. J. Rojas, *Chem. Rev.*, 2010, **110**, 3479–3500.
8 W. Hamad, *Can. J. Chem. Eng.*, 2006, **84**, 513–519.
9 B. L. Peng, N. Dhar, H. L. Liu and K. C. Tam, *Can. J. Chem. Eng.*, 2011, **89**, 1191–1206.
10 H. Sehaqui, Z. Qi, O. Ikkala and L. A. Berglund, *Biomacromolecules*, 2011, **12**, 3638–3644.
11 M. A. Hubbe, O. J. Rojas, L. A. Lucia, M. Sain and T. A. Forest, *BioResources*, 2008, **3**, 929–980.
12 N. Durán, A. P. Lemes and A. B. Seabra, *Recent Pat. Nanotechnol.*, 2012, **6**, 16–28.
13 A. Dufresne, *Molecules*, 2010, **15**, 4111–4128.
14 A. Kaboorani, B. Riedl, P. Blanchet, M. Fellin, O. Hosseinaei and S. Wang, *Eur. Polym. J.*, 2012, **48**, 1829–1837.
15 J. Iang, Z. Jiang, K. Ca, and R. Berry, US20110293932 A1 Patent application, 2011, 1.
16 J. Han, C. Zhou, Y. Wu, F. Liu and Q. Wu, *Biomacromolecules*, 2013, **14**, 1529–1540.
17 R. Dash, Y. Li and A. J. Ragauskas, *Carbohydr. Polym.*, 2012, **88**, 789–792.
18 J. P. F. Lagerwall, C. Schütz, M. Salajkova, J. Noh, J. Hyun Park, G. Scalia and L. Bergström, *NPG Asia Mater.*, 2014, **6**, e80.
19 C. D. Edgar and D. G. Gray, *Cellulose*, 2001, 5–12.
20 H. Tang, B. Guo, H. Jiang, L. Xue, B. Li, X. Cao, Q. Zhang and P. Li, *Cellulose*, 2013, **20**, 2667–2674.
21 J. Pan, W. Hamad and S. K. Straus, *Macromolecules*, 2010, **43**, 3851–3858.
22 S. Belbekhouche, J. Bras, G. Siqueira, C. Chappey, L. Lebrun, B. Khelifi, S. Marais and A. Dufresne, *Carbohydr. Polym.*, 2011, **83**, 1740–1748.
23 E. Borovitskaya and M. Shur, *Selective Topics in Electronics and Systems*, 2002.
24 R. F. Kazarinov and R. A. Suris, *Soviet Physics - Semiconductors*, 1971, **5**, 707.
25 A. Yoffe, *Adv. Phys.*, 2001, 1–208.
26 N. N. Ledentsov, V. M. Ustinov, V. A. Shchukin, P. S. Kop'ev, Z. I. Alferov and D. Bimberg, *Semiconductors*, 1998, **32**, 343–365.
27 E. Biolatti, R. C. Iotti, P. Zanardi and F. Rossi, *Phys. Rev. Lett.*, 2000, **85**, 5647–5650.
28 A. Marent, M. Geller, A. Schliwa, D. Feise, K. Pötschke, D. Bimberg, N. Akçay and N. Öncan, *Appl. Phys. Lett.*, 2007, **91**, 242109.
29 M. Gr, *Nature*, 2001, 414.
30 I. Robel, V. Subramanian, M. Kuno and P. V Kamat, *J. Am. Chem. Soc.*, 2006, **128**, 2385–2393.
31 R. Turton, *The Quantum Dot: A Journey into the Future of Microelectronics*, 1996.
32 S. Coe, W. Wing-Keung, M. Bawendi and V. Bulovic, *Nature*, 2002, **420**, 3–6.
33 V. L. Colvin, M. Schlamp and A. Allvisatos, *Nature*, 1994, **370**, 354.
34 R. Ye, C. Xiang, J. Lin, Z. Peng, K. Huang, Z. Yan, N. P. Cook, E. L. G. Samuel, C.-C. Hwang, G. Ruan, G. Ceriotti, A.-R. O. Raji, A. A. Martí and J. M. Tour, *Nat. Commun.*, 2013, **4**, 2943.
35 C. Cassidy, J. Kioseoglou, V. Singh, P. Grammatikopoulos, C. Lal and M. Sowwan, *Appl. Phys. Lett.*, 2014, **104**, 161903.

36 N. Tessler, V. Medvedev, M. Kazes, S. Kan and U. Banin, *Science*, 2002, **295**, 1506–1508.
37 L. Levina, V. Sukhovatkin, S. Musikhin, S. Cauchi, R. Nisman, D. P. Bazett-Jones and E. H. Sargent, *Adv. Mater.*, 2005, **17**, 1854–1857.
38 S. A. McDonald, G. Konstantatos, S. Zhang, P. W. Cyr, E. J. D. Klem, L. Levina and E. H. Sargent, *Nat. Mater.*, 2005, **4**, 138–142.
39 V. L. Colvin and A. N. Goldstein, *J. Am. Chem. Soc.*, 1992, **8721657**, 5221–5230.
40 M. Achermann, M. A. Petruska, S. Kos, D. L. Smith, D. D. Koleske and V. I. Klimov, *Nature*, 2004, **429**, 642–646.
41 D. Cahen, R. Naaman and Z. Vager, *Adv. Funct. Mater.*, 2005, **15**, 1571–1578.
42 M. T. Neves-Petersen, G. P. Gajula and S. B. Petersen, *Mol. Photochem.: Var. Aspects*, 2011, 125–158.
43 C. Turek and F. C. Stintzing, *Compr. Rev. Food Sci. Food Saf.*, 2013, **12**, 40–53.
44 E. Chiel, Y. Messika, S. Steinberg and Y. Antignus, *Biocontrol*, 2006, **51**, 65–78.
45 N. Katsoulas, T. Bartzanas, C. Nikolaou, and C. Kittas, *Structures and Environmental Technologies*, 2012, p. P-2280.
46 R. D. Mears, J. R. William and J. C. Simpkins, *Am. Soc. Agric. Eng., Pap.*, 1974, NA74–112.
47 L. Pranger and R. Tannenbaum, *Macromolecules*, 2008, **41**, 8682–8687.
48 D. Sridevi and K. V. Rajendran, *International Journal of Nanotechnology and Applications*, 2009, **32**, 165–168.
49 M. A. Gondal and M. A. Dastageer, *Appl. Phys. B*, 2011, **106**, 419–424.
50 X.-M. Chen, Y. Ji, X.-Y. Gao and X.-W. Zhao, *Chin. Phys. B*, 2012, **21**, 116801.
51 J. Zhou, N. S. Xu and Z. L. Wang, *Adv. Mater.*, 2006, **18**, 2432–2435.
52 X. Li, L. Wang, Y. Fan, Q. Feng and F. Cui, *J. Nanomater.*, 2012, **2012**, 1–19.
53 J.-H. Park, L. Gu, G. von Maltzahn, E. Ruoslahti, S. N. Bhatia and M. J. Sailor, *Nat. Mater.*, 2009, **8**, 331–336.
54 Y. Yin and A. P. Alivisatos, *Nature*, 2005, **437**, 664–670.
55 R. M. Nielsen, S. Murphy, C. Strebel, M. Johansson, I. Chorkendorff and J. H. Nielsen, *J. Nanopart. Res.*, 2009, **12**, 1249–1262.
56 V. Srikant and D. R. Clarke, *J. Appl. Phys.*, 1998, **83**, 5447.
57 R. Yousefi, A. K. Zak and F. Jamali-Sheini, *Ceram. Int.*, 2013, **39**, 1371–1377.
58 T. Huq, S. Salmieri, A. Khan, R. A. Khan, C. Le Tien, B. Riedl, C. Fraschini, J. Bouchard, J. Uribe-Calderon, M. R. Kamal and M. Lacroix, *Carbohydr. Polym.*, 2012, **90**, 1757–1763.
59 Y. Sun, L. Lin, H. Deng, J. Li, B. He, R. Sun and P. Ouyang, *BioResources*, 2008, **3**, 297–315.
60 R. Kitamura, L. Pilon and M. Jonasz, *Appl. Opt.*, 2007, **46**, 8118–8133.

Bibliography

(1) Kelvin, L. W. T. *The Molecular Tactics of a Crystal*; Clarendon Press, 1893.

(2) Barron, L. D. In *Chirality at the Nanoscale*; Amabilino, D. B., Ed.; Wiley-VCH Verlag GmbH & Co. KGaA, 2009; pp 1–27.

(3) Farago, P. S. *J. Phys. B At. Mol. Phys.* **1980**, *13* (18), L567–L571.

(4) Farago, P. S. *J. Phys. B At. Mol. Phys.* **1981**, *14* (22), L743–L748.

(5) Rich, A.; Van House, J.; Hegstrom, R. A. *Phys. Rev. Lett.* **1982**, *48* (19), 1341–1344.

(6) Campbell, D. M.; Farago, P. S. *J. Phys. B At. Mol. Phys.* **1987**, *20* (19), 5133–5143.

(7) Mayer, S.; Kessler, J. *Phys. Rev. Lett.* **1995**, *74* (24), 4803–4806.

(8) Wei, J. J.; Schafmeister, C.; Bird, G.; Paul, A.; Naaman, R.; Waldeck, D. H. *J. Phys. Chem. B* **2006**, *110* (3), 1301–1308.

(9) Göhler, B.; Hamelbeck, V.; Markus, T. Z.; Kettner, M.; Hanne, G. F.; Vager, Z.; Naaman, R.; Zacharias, H. *Science* **2011**, *331* (6019), 894–897.

(10) L.J.A.Rikken Geert. *Science* **2011**, *331*, 864–865.

(11) Xie, Z.; Xie, Z.; Markus, T. Z.; Cohen, S. R.; Vager, Z.; Gutierrez, R.; Naaman, R. *Nano Lett.* **2011**, *11* (11), 4652–4655.

(12) Faraday, M. *Philos. Trans. R. Soc. London* **1857**, *147*, 145–181.

(13) Reed, G. . *Silicon Photonics*; Reed, G. T., Ed.; John Wiley & Sons, Ltd: Chichester, UK, 2008.

(14) Shah, a. V.; Platz, R.; Keppner, H. *Sol. Energy Mater. Sol. Cells* **1995**, *38* (1-4), 501–520.

(15) Carlson, R. O. *Phys. Rev.* **1955**, *100* (4), 1075–1078.

(16) Ernst, K.-H. *Phys. status solidi* **2012**, *249* (11), 2057–2088.

(17) Barron, L. D. *Molecular Light Scattering and Optical Activity*; Cambridge University Press, 2004.

(18) Eremko, a. a.; Loktev, V. M. *Phys. Rev. B - Condens. Matter Mater. Phys.* **2013**, *88* (16), 1–5.

(19) Krstić, V.; Rikken, G. L. J. a. *Chem. Phys. Lett.* **2002**, *364* (1-2), 51–56.

(20) Yeganeh, S.; Ratner, M. a.; Medina, E.; Mujica, V. *J. Chem. Phys.* **2009**, *131* (1).

(21) Medina, E.; López, F.; Ratner, M. A.; Mujica, V. *EPL (Europhysics Lett.* **2012**, *99* (1), 17006.

(22) Gutierrez, R.; Díaz, E.; Naaman, R.; Cuniberti, G. *Phys. Rev. B* **2012**, *85* (8), 081404.

(23) Gutierrez, R.; Cuniberti, G. *Acta Phys. Pol. A* **2015**, *127* (2), 185–191.

(24) Guo, A.-M.; Sun, Q. *Phys. Rev. Lett.* **2012**, *108* (21), 218102.

(25) Guo, A. M.; Sun, Q. F. *Phys. Rev. B - Condens. Matter Mater. Phys.* **2012**, *86* (11), 1–6.

(26) Gersten, J.; Kaasbjerg, K.; Nitzan, A. *J. Chem. Phys.* **2013**, *139* (11).

(27) Thomas, L. H. *Nature* **1926**, *117* (2945), 514–514.

(28) Naaman, R.; Waldeck, D. H. *J. Phys. Chem. Lett.* **2012**.

(29) Winkler, D. R. In *Spin--Orbit Coupling Effects in Two-Dimensional Electron and Hole Systems*; Springer Tracts in Modern Physics; Springer Berlin Heidelberg, 2003; pp 61–68.

(30) Naaman, R.; Waldeck, D. H. *J. Phys. Chem. Lett.* **2012**, *3* (16), 2178–2187.

(31) Qu, L.; Peng, X. *J. Am. Chem. Soc.* **2002**, *124* (9), 2049–2055.

(32) Nanocrystallites, T. S.; Murray, C. B.; Noms, D. J.; Bawendi, M. G. **1993**, No. 4, 8706–8715.

(33) Peng, X.; Manna, L.; Yang, W.; Wickham, J.; Scher, E.; Kadavanich, A.; Alivisatos, A. *Nature* **2000**, *404* (6773), 59–61.

(34) Manna, L.; Scher, E. C.; Alivisatos, a. P. *J. Am. Chem. Soc.* **2000**, *122* (51), 12700–12706.

(35) Pankove, J. I. *Optical Processes in Semiconductors*; Courier Corporation, 1971.

(36) Klimov, V. *Nanocrystal quantum dots*; 2010.

(37) Efros, A. *Sov. Phys. …* **1982**.

(38) Baldereschi, A.; Lipari, N. O. *Phys. Rev. B* **1973**, *8* (6), 2697–2709.

(39) Klimov, V. I. *Nanocrystal Quantum Dots Second edition*; 2010.

(40) Nirmal, M.; Norris, D. J.; Kuno, M.; Bawendi, M. G.; Efros, A. L.; Rosen, M. *Phys. Rev. Lett.* **1995**, *75* (20), 3728–3731.

(41) Nahálková, P.; Sprinzl, D.; Malý, P.; Němec, P.; Gladilin, V. N.; Devreese, J. T. *Phys. Rev. B* **2007**, *75* (11), 113306.

(42) Vinattieri, A.; Shah, J.; Damen, T. C.; Kim, D. S.; Pfeiffer, L. N.; Maialle, M. Z.; Sham, L. J. *Phys. Rev. B* **1994**, *50* (15), 10868–10879.

(43) Pikus, G.E. and Bir, G. L. *Sov. Phys. JETP* **1971**, *33* (1), 108–114.

(44) Ma, H.; Jin, Z.; Zhang, Z.; Li, G.; Ma, G. *J. Phys. Chem. A* **2012**, *116* (9), 2018–2023.

(45) Němec, P.; Nahálková, P.; Sprinzl, D.; Malý, P.; Gladilin, V. N.; Devreese, J. T. *Phys. status solidi* **2006**, *3* (12), 4291–4294.

(46) Marqusee, S.; Robbins, V. H.; Baldwin, R. L. *Proc. Natl. Acad. Sci.* **1989**, *86* (14), 5286–5290.

(47) Carmeli, I.; Skakalova, V.; Naaman, R.; Vager, Z. *Angew. Chemie* **2002**, *114* (5), 787–790.

(48) Kennedy, D. F.; Crisma, M.; Toniolo, C.; Chapman, D. *Biochemistry* **1991**, *30* (26), 6541–6548.

(49) Miura, Y.; Kimura, S.; Imanishi, Y.; Umemura, J. *Langmuir* **1998**, *14* (24), 6935–6940.

(50) Winkler, R. *Spin-orbit Coupling Effects in Two-Dimensional Electron and Hole Systems, Issue 191*; Springer Science & Business Media, 2003.

(51) Uskov, a. V.; Boucher, Y.; Le Bihan, J.; McInerney, J. *Appl. Phys. Lett.* **1998**, *73* (11), 1499–1501.

(52) Barker, A. S. *Phys. Rev. B* **1973**, *8* (12), 5418–5426.

(53) Donegá, C. D. M.; Bode, M.; Meijerink, A. **2006**, No. April, 1–9.

(54) Syperek, M.; Yakovlev, D.; Yugova, I.; Misiewicz, J.; Sedova, I.; Sorokin, S.; Toropov, a.; Ivanov, S.; Bayer, M. *Phys. Rev. B* **2011**, *84* (8), 1–8.

(55) Zhang, Z.; Jin, Z.; Ma, H.; Xu, Y.; Lin, X.; Ma, G.; Sun, X. *Phys. E Low-Dimensional Syst. Nanostructures* **2014**, *56*, 85–89.

(56) Carmeli, I.; Kumar, K. S.; Heifler, O.; Carmeli, C.; Naaman, R. *Angew. Chemie* **2014**, *126* (34), 9099–9104.

(57) Dor, O. Ben; Morali, N.; Yochelis, S.; Baczewski, L. T.; Paltiel, Y. *Nano Lett.* **2014**, *14* (11), 6042–6049.

(58) Heux, L.; Chauve, G.; Bonini, C. **2000**, *07493* (19), 8210–8212.

(59) Beck-Candanedo, S.; Roman, M.; Gray, D. G. *Biomacromolecules* **2005**, *6* (2), 1048–1054.

(60) Roman, M.; Winter, W. T. *Biomacromolecules* **2004**, *5* (5), 1671–1677.

(61) Araki, J.; Kuga, S. **2001**, No. 14, 4493–4496.

(62) Bondeson, D.; Mathew, A.; Oksman, K. *Cellulose* **2006**, *13* (2), 171–180.

(63) Revol, J. F.; Bradford, H.; Giasson, J.; Marchessault, R. H.; Gray, D. G. *Int. J. Biol. Macromol.* **1992**, *14* (3), 170–172.

(64) Habibi, Y.; Lucia, L. a; Rojas, O. J. *Chem. Rev.* **2010**, *110* (6), 3479–3500.

(65) Hamad, W. **2006**, *84* (OCTOBER), 513–519.

(66) Peng, B. L.; Dhar, N.; Liu, H. L.; Tam, K. C. *Can. J. Chem. Eng.* **2011**, *89* (5), 1191–1206.

(67) Sehaqui, H.; Qi, Z.; Ikkala, O.; A. Berglund, L. Strong and Tough Cellulose Nanopaper with High Specific Surface Area and Porosity http://pubs.acs.org/doi/pdf/10.1021/bm2008907 (accessed Sep 18, 2014).

(68) Hubbe, M. A.; Rojas, O. J.; Lucia, L. A.; Sain, M.; Forest, T. A. **2008**, *3*, 929–980.

(69) Durán, N.; Lemes, A. P.; Seabra, A. B. *Recent Pat. Nanotechnol.* **2012**, *6* (1), 16–28.

(70) Dufresne, A. *Molecules* **2010**, *15* (6), 4111–4128.

(71) Kaboorani, A.; Riedl, B.; Blanchet, P.; Fellin, M.; Hosseinaei, O.; Wang, S. *Eur. Polym. J.* **2012**, *48* (11), 1829–1837.

(72) Iang, J.; Jiang, Z.; Ca, K.; Berry, R. **2011**, *1* (61).

(73) Han, J.; Zhou, C.; Wu, Y.; Liu, F.; Wu, Q. *Biomacromolecules* **2013**, *14* (5), 1529–1540.

(74) Dash, R.; Li, Y.; Ragauskas, A. J. *Carbohydr. Polym.* **2012**, *88* (2), 789–792.

(75) Lagerwall, J. P. F.; Schütz, C.; Salajkova, M.; Noh, J.; Hyun Park, J.; Scalia, G.; Bergström, L. *NPG Asia Mater.* **2014**, *6* (1), e80.

(76) Edgar, C. D.; Gray, D. G. **2001**, 5–12.

(77) Tang, H.; Guo, B.; Jiang, H.; Xue, L.; Li, B.; Cao, X.; Zhang, Q.; Li, P. *Cellulose* **2013**, *20* (6), 2667–2674.

(78) Pan, J.; Hamad, W.; Straus, S. K. *Macromolecules* **2010**, *43* (8), 3851–3858.

(79) Belbekhouche, S.; Bras, J.; Siqueira, G.; Chappey, C.; Lebrun, L.; Khelifi, B.; Marais, S.; Dufresne, A. *Carbohydr. Polym.* **2011**, *83* (4), 1740–1748.

(80) Neves-petersen, M. T.; Gajula, G. P.; Petersen, S. B. **2011**.

(81) Turek, C.; Stintzing, F. C. *Compr. Rev. Food Sci. Food Saf.* **2013**, *12* (1), 40–53.

(82) Chiel, E.; Messika, Y.; Steinberg, S.; Antignus, Y. *Biocontrol* **2006**, *51* (1), 65–78.

(83) Katsoulas, N.; Bartzanas, T.; Nikolaou, C.; Kittas, C. **2004**.

(84) Mears; David, R.; William, J. R.; Simpkins, J. C. *Am. Soc. Agric. Eng.* **1974**, *NA74-112*.

(85) Park, Y.; Choong, V.; Gao, Y.; Hsieh, B. R.; Tang, C. W. *Appl. Phys. Lett.* **1996**, *68* (19), 2699.

(86) Derry, G. N.; Ji-Zhong, Z. *Phys. Rev. B* **1989**, *39* (3), 1940–1941.

(87) Anderson, P. A. *Phys. Rev.* **1959**, *115* (3), 553–554.

(88) Sheldon, M. T. *Lawrence Berkeley Natl. Lab.* **2010**.

(89) Anikeeva, P.; Anikeeva, P.; Halpert, J.; Halpert, J.; Bawendi, M.; Bawendi, M. *Nano Lett* **2007**, 0–4.

תקציר

הפרדת מטען הינו תהליך בסיסי הנמצא בשימוש במגוון רחב של רכיבים אופטו-אלקטרוניים, כגון תאים סולאריים ובגלאים אופטיים. תת-משפחה של רכיבים אלו הם תאים פוטו-וולטאים, שהם מערכות הפועלות באמצעות אנרגיית אור. ברבים מהתקנים אלה, תהליך הפרדת המטען מצריך יצירת צומת P-N בין שני אזורי סימום שונים של מוליך למחצה מאולח. אילוח של מל"מ הינו תהליך מוגבל בגדלים ננומטרים בשל מספר קטן יותר של אטומים המרכיבים את הגביש, ולכן יצירת צמתי N-P מוגבלת בסקלת הננו.

בשנים האחרונות, מחקרים בנושא מעבר אלקטרונים במולקולות אורגניות כיראליות הראו שניתן לייחס למולקולות תכונות קוונטיות, כגון רמות אנרגתיות בדידות וכן סינון ספין של האלקטרונים, כל זה בטמפרטורות החדר. תכונת סינון הספין אשר נמצאה להיות יעילה ביותר והיא מיוחסת לאינטרקציית ספין-מסילה חזקה בין האלקטרון לפוטנציאל המושרה ע"י המולקולה, והיא נקראת אפקט סינון הספין המושרה ע"י כיראליות (CISS).

ננו-גבישים מוליכים למחצה הינם חומרים בעלי פונציאל רב בשימוש בהתקנים אופטיים. הם בעלי גמישות לכיוונון התכונות האופטיות והחשמליות שלהם ע"י שינוי גודל בגביש, צורתו והרכבו. ע"י שימוש בננו-גבישים מל"מים ותכונות סינון הספין של אלקטרונים העוברים דרך מולקולות כיראליות, אנו מדגימים במחקר זה יצירת הפרדת מטען בהתקנים המורכבים משכבות דקות ספוחות של מולקולות כיראליות וננו-גבישים מל"מים. על ידי ביצוע עירורים אופטיים מקוטבים של הננו-גבישים ומדידת תגובות הזרם של ההתקן אנו מוכיחים שהאפקט קיים בסקלה הננומטרית. הקיטוב המעגלי של האור המעורר יוצר ספין מוגדר למטענים המעוררים ובכך משפיע על הסיכוי שלהם לעבור דרך השכבה של המולקולות הכיראליות.

תוצאות המדידות מראות שינויים משמעותיים בתגובת הזרם המיוחסת לאפקט ה-CISS היוצר הפרדת מטען בטמפרטורת החדר. ההתקנים הללו יכולים בעתיד להיות מיוצרים בסקלות קטנות יותר, והוורסטיליות של גודל הננו-גבישים מאפשרת התאמה של ספקטרום הבליעה האופטית של ההתקן. טכנולוגיה זו עשויה לשמש בעתיד ליצירת ציפויים אקטיביים הבולעים אור ויוצרים הפרדת מטען.

האוניברסיטה העברית בירושלים

הפקולטה למתמטיקה ולמדעי הטבע

המחלקה לפיסיקה יישומית

יצירת הפרדת מטען ננומטרית באמצעות שימוש במולקולות כיראליות

ניר פאר

בהדרכת: פרופ' יוסי פלטיאל

עבודת גמר לתואר מוסמך במדעי הטבע

יולי 2015

תשע"ה